A Thesis Submitted to the Sylhet Engineering College for the Degree of
Bachelor of Science in Electrical and Electronic Engineering

Hybrid Intelligent MPPT for Stand-Alone PV-Battery Systems: ANN-FOPID Control

By
Banashree Debi Popy
Al Amin Rabbi
&
Md. Nahidul Islam

Supervised by
Md. Faiyaj Ahmed Limon
Lecturer
Department of Electrical and Electronic Engineering
Leading University, Sylhet

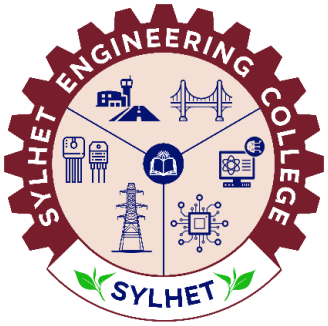

June, 2025
Sylhet Engineering College, Sylhet
Affiliated with
Shahjalal University of Science & Technology (SUST)

CERTIFICATION

The thesis titled **"Hybrid Intelligent MPPT for Stand-Alone PV-Battery Systems: ANN-FOPID Control"** submitted by **Banashree Debi Popy, Al Amin Rabbi** and **Md. Nahidul Islam** ; Student ID: **2019338562, 2019338554**, and **2019338559**; Session **2019-20**, to the Department of Electrical and Electronic Engineering, Sylhet Engineering College, has been accepted as satisfactory in partial fulfillment of the requirement for the Degree of Bachelor of Science in Electrical and Electronic Engineering and approved as to its style and contents.

BOARD OF EXAMINERS

_____
Md. Shahid Iqbal — Chairman
Assistant Professor and Head
Department of Electrical and Electronic Engineering
Sylhet Engineering College, Sylhet.

_____
Md. Faiyaj Ahmed Limon — Supervisor
Lecturer
Department of Electrical and Electronic Engineering
Leading University , Sylhet.

_____
Salman Fazle Rabby — Member
Assistant Professor
Department of Electrical and Electronic Engineering
Sylhet Engineering College, Sylhet.

_____
Apurba Biswas — Member
Assistant Professor
Department of Electrical and Electronic Engineering
Sylhet Engineering College, Sylhet.

_____

Md. Ashraful Alam — Member
Lecturer
Department of Electrical and Electronic Engineering
Sylhet Engineering College, Sylhet.

_____

Mahedi Kamal Ahmed — Member
Lecturer
Department of Electrical and Electronic Engineering
Sylhet Engineering College, Sylhet.

_____

Arif Ahammad — Member (External)
Assistant Professor
Department of Electrical and Electronic Engineering
Shahjalal University of Science & Technology, Sylhet.

Acknowledgements

First and foremost, we offer our deepest gratitude to the Almighty, whose silent presence and infinite grace have been the guiding light throughout our life. In every quiet triumph and every hidden struggle, it is by His will that we have found strength, clarity, and purpose. This work is a humble reflection of the countless blessings He has bestowed upon us, often unseen yet always deeply felt.

We would like to express our deepest appreciation to our respected thesis supervisor, **Md. Faiyaj Ahmed Limon**, for his constant support, invaluable guidance, and constructive feedback. His encouragement and insightful suggestions have greatly enriched our work and learning experience.

We would also like to extend our sincere gratitude to **Md. Shahid Iqbal**, **Salman Fazle Rabby,**

Md. Ashraful Alam, and who have been our respected course teachers throughout our academic journey. Their dedication to teaching, depth of knowledge, and continuous encouragement have left a profound impact on our learning experience. Each of them, in their unique way, has helped shape our academic foundation and inspired us to pursue excellence with confidence and clarity.

Lastly, with all our love and respect, we express our deepest gratitude to our beloved parents, whose unconditional love, endless sacrifices, and constant prayers have always been the source of our strength. Their unwavering belief in us has been the foundation of all our achievements.

Abstract

The global shift to renewable energy underscores the critical role of photovoltaic (PV) systems, where efficient Maximum Power Point Tracking (MPPT) optimizes power extraction under varying irradiance and temperature conditions. Conventional MPPT methods, using static or lookup-based reference voltage (V_{ref}) estimation, lack adaptability to rapidly changing environments, leading to suboptimal power extraction. Hybrid controllers introduce computational complexity, while limited Artificial Neural Network (ANN) research for dynamic V_{ref} prediction restricts cost-sensitive standalone PV applications. This study proposes a streamlined, non-hybrid MPPT framework integrating a Feedforward Artificial Neural Network (FNN) for real-time V_{ref} prediction with metaheuristic-optimized Proportional-Integral-Derivative (PID) and Fractional-Order PID (FOPID) controllers. A pre-trained FNN maps real-time irradiance and temperature to optimal voltages, supported by eight metaheuristic algorithms (PSO, GA, DE, CS, ABC, ACO, GWO, WOA) tuning controllers to minimize the Integral of Time-weighted Absolute Error (ITAE). Tested across six scenarios, including slow diurnal variations and extreme irradiance shifts, the simulated standalone PV-battery system with a DC-DC buck converter uses FNN-predicted V_{ref} for duty cycle adjustments. The WOA-tuned FOPID outperformed DE-PID, achieving an average 0.05% higher efficiency (up to 0.09%), 64.9% reduced energy loss (up to 93.6% under rapid irradiance changes), and 0.20% lower ITAE (up to 2.4%). WOA-FOPID's tracking time was 14.9% slower on average due to an outlier case (-1100%), but achieved up to 32.1% faster tracking in dynamic conditions. DE-PID exhibited lower ripple (~0.1% vs. 1.15–1.67%) and overshoot (~2.77% vs. 3.00%) in most scenarios, highlighting its stability. The ANN-FOPID framework provides a robust, efficient, and feasible MPPT solution, significantly enhancing standalone PV performance.

Keywords: PV system, MPPT, V_{ref} prediction, ANN, PID, FOPID, Metaheuristic Optimization, WOA.

Table of Contents

List of Figures

List of Tables

Chapter 1: Introduction

1.1 Background of Renewable Energy and MPPT in PV Systems

The accelerating global energy demand, driven by rapid industrialization, urbanization, and population growth, has raised significant concerns regarding the sustainability and environmental impact of conventional fossil fuel-based energy sources. With the depletion of fossil fuels and the associated environmental degradation, a global transition toward renewable energy resources has become imperative. Among various renewable energy options, photovoltaic (PV) systems have gained widespread adoption due to their sustainability, simplicity, ease of installation, and low operational costs [1-2].

PV systems, classified as standalone, grid-connected, or hybrid, serve diverse applications from remote areas to urban grids, setting the stage for addressing MPPT challenges in optimizing power extraction.

Despite their advantages, PV systems face significant challenges. The power output of PV panels is inherently nonlinear and highly sensitive to environmental variables, especially solar irradiance and temperature, which fluctuate unpredictably throughout the day [3-4]. Furthermore, varying load demands introduce additional complexity by causing mismatches between energy generation and consumption, which adversely affect the overall reliability and energy efficiency of standalone PV systems [4]. To overcome these challenges and optimize power extraction, Maximum Power Point Tracking (MPPT) techniques have become a crucial component in PV system design.

1.2 Maximum Power Point Tracking: Principle and Importance

To address the inherent variability in solar irradiance and temperature, Maximum Power Point Tracking (MPPT) techniques are integral to photovoltaic (PV) systems. MPPT ensures that the system continuously operates at its optimal power point by dynamically adjusting the operating conditions in real time. This enables consistent and efficient energy extraction, improving overall system performance, reliability, and energy yield [1], [5].

MPPT maximizes PV power output by adjusting the operating voltage via DC-DC converter duty cycles, using a reference voltage (V_{ref}) to track the maximum power point (MPP) under

varying conditions, with techniques like Perturb and Observe (P&O), Incremental Conductance (INC), and intelligent methods such as Artificial Neural Networks (ANN) and metaheuristic algorithms offering trade-offs in speed, stability, and complexity.

1.3 Reference Voltage (V_{ref}): Concept and Relevance in MPPT

The reference voltage (V_{ref}), the estimated voltage at the Maximum Power Point (MPP) of a photovoltaic (PV) panel under specific irradiance and temperature conditions, is crucial for accurate and responsive Maximum Power Point Tracking (MPPT). By steering the PV system toward V_{ref}, MPPT strategies enhance tracking speed and stability, minimizing oscillations under varying environmental conditions.

Unlike traditional static V_{ref} estimation methods, such as fixed fractions of open-circuit voltage, modern intelligent models and optimization-based approaches predict V_{ref} dynamically using sensor data, enabling efficient duty cycle control in DC–DC converters or optimization frameworks for robust power tracking.

1.4 Artificial Neural Network-Based V_{ref} Prediction

Artificial Neural Networks (ANNs) dynamically predict the reference voltage (V_{ref}) for Maximum Power Point Tracking (MPPT) in PV systems, adapting to varying irradiance and temperature conditions to enhance tracking accuracy over static methods. Feedforward Neural Networks (FNNs), preferred for their simplicity and efficiency, map input variables (e.g., irradiance, temperature) to V_{ref}, enabling fast convergence and reliable performance in embedded PV systems.

1.5 Control Strategies for V_{ref} Tracking in PV Systems

Accurate tracking of the reference voltage (V_{ref}) in photovoltaic (PV) systems, achieved by regulating DC-DC converter duty cycles, relies on Proportional-Integral-Derivative (PID) and Fractional-Order PID (FOPID) controllers to ensure fast and stable convergence to the maximum power point (MPP) under dynamic conditions. While PID offers simplicity for stable systems, FOPID's fractional calculus enhances flexibility to handle nonlinearities, with optimal performance requiring intelligent tuning via metaheuristic algorithms for robust, efficient MPPT.

1.6 Motivation and Significance of the Work

With the rising demand for clean and sustainable energy, photovoltaic (PV) systems have become a vital part of modern renewable energy solutions. However, the power output of PV systems is highly dependent on variable environmental factors such as solar irradiance and temperature, making Maximum Power Point Tracking (MPPT) crucial for efficient energy harvesting[5].

Controller-based MPPT techniques, such as conventional PID and FOPID controllers, have been widely adopted due to their simplicity and effectiveness. Despite the enhanced performance and robustness offered by FOPID controllers in handling system nonlinearities and transient dynamics, these conventional controllers still face significant challenges in maintaining optimal performance under rapidly changing environmental and load conditions [6-10].

To address these challenges, real-time adaptive control strategies and metaheuristic optimization algorithms have been explored for dynamic tuning of controller parameters [11-15]. Nevertheless, a key limitation persists. many MPPT approaches still rely on fixed or model-based V_{ref} generation methods, which are derived from static ratios, analytical models, or predefined algorithms. These approaches do not adapt dynamically to real-time variations in irradiance and temperature, significantly constraining the controller's responsiveness and tracking accuracy, and ultimately reducing energy conversion efficiency using energy conversion efficiency [16-18]

Motivated by this gap, this research proposes an ANN-based adaptive MPPT framework to dynamically predict V_{ref}, enhancing controller performance while maintaining simplicity and improving efficiency for standalone PV systems under fluctuating conditions.

1.7 Research Gap and Problem Statement

Proportional–Integral–Derivative (PID) and Fractional Order PID (FOPID) controllers are widely used in photovoltaic (PV) applications due to their straightforward implementation and control stability. While FOPID extends the capabilities of conventional PID by offering better robustness and tuning flexibility, both controllers face performance degradation in highly

nonlinear and dynamic PV environments, particularly under fluctuating irradiance, temperature, and load conditions [8 -12] ,[18-21].

To improve adaptability and tracking performance, various hybrid control strategies have emerged—often integrating metaheuristic optimization algorithms [22] fuzzy logic [23-24], or artificial neural networks (ANNs) [25]. Although these hybrid approaches improve performance, they increase complexity and computational demands, reducing feasibility for low-cost embedded PV systems.

Another fundamental limitation in many maximum power point tracking (MPPT) systems is the use of static or predetermined reference voltage (V_{ref}) generation methods, such as fixed ratios [16] or lookup-based estimations [19-20]. These techniques lack adaptability to real-time environmental changes, and adaptive solutions often rely on complex hybrid architectures, compromising simplicity and scalability.

Despite the growing focus on hybrid MPPT solutions, limited attention has been given to non-hybrid, intelligent controller architectures that combine simplicity with adaptability. In particular, a standalone ANN for dynamic V_{ref} prediction with metaheuristic-optimized PID or FOPID controllers remains largely unexplored in existing literature [25-26].

To address this gap, this research proposes a non-hybrid ANN for real-time V_{ref} prediction with metaheuristic-tuned PID/FOPID controllers, enhancing MPPT performance while preserving simplicity.

1.8 Objectives of the Study

The main goal of this study is to enhance MPPT performance using ANN-based V_{ref} prediction and metaheuristic-tuned PID/FOPID controllers. The specific objectives are.

1. Develop an ANN model to predict V_{ref} dynamically for MPPT.
2. Design conventional PID and FOPID controllers for non-hybrid MPPT.
3. Tune PID and FOPID controller parameters using metaheuristic algorithms.
4. Compare the performance of optimized PID and FOPID controllers under varying conditions, assessing FOPID's advantages.

1.9 Thesis Structure

This thesis is organized into six chapters to systematically present the research on the proposed ANN-FOPID MPPT framework for standalone PV-battery systems:

Chapter 1: Introduction, provides the background, significance, and motivation for the study, introducing renewable energy, MPPT, and the proposed ANN-FOPID approach, along with the research gap and objectives.

Chapter 2: Literature Review reviews classical, hybrid, and intelligent MPPT techniques, highlighting their strengths, limitations, and the need for a simplified, adaptive solution.

Chapter 3: System's Control Scheme and Methodology describes the standalone PV-battery architecture, the ANN-based V_{ref} prediction, PID/FOPID control strategies, and metaheuristic tuning using the ITAE criterion.

Chapter 4: Implementation details the PV system model battery configuration, buck converter design, FNN architecture, and metaheuristic optimization, including six test scenarios for performance evaluation.

Chapter 5: Result and Analysis presents simulation results, comparing PID and FOPID controllers across efficiency, energy loss, tracking time, ripple, overshoot, and ITAE, with a focus on WOA-FOPID vs. DE-PID.

Chapter 6: Conclusion and Future Work summarizes key findings underscores the superiority of the ANN-FOPID framework, and proposes future research directions, including hardware validation and advanced neural network integration.

1.10 Summary

This chapter investigates classical, hybrid, and intelligent MPPT techniques for photovoltaic systems, highlighting trade-offs between simplicity, efficiency, and adaptability. While intelligent and metaheuristic methods offer high accuracy and fast tracking, they often face real-time implementation challenges due to complexity and computational demands. To address these limitations, the proposed method introduces an adaptive, low-complexity MPPT approach with intelligent V_{ref} prediction, ensuring efficient and robust performance under dynamic conditions.

Chapter 2: Literature Review

2.1. Classical MPPT Techniques (Baseline)

MATLAB/Simulink simulations evaluate Perturb and Observe (P&O) and Incremental Conductance (IC) under constant and variable irradiance. IC achieves faster convergence (0.25 s vs. 0.35 s), higher efficiency (97.93% vs. 97.77%), and no oscillations, unlike P&O. While P&O is simpler, IC's complexity limits low-cost PV system use, highlighting the need for adaptive, low-complexity MPPT solutions, which this research addresses [27]. An improved P&O algorithm with dynamic step-size and boundary conditions enhances stability, achieving 99.4% efficiency vs. 97.5% for standard P&O, using software-only implementation. Validated only for buck–boost converters, it requires careful threshold tuning and lacks intelligent MPPT comparison, limiting dynamic condition applicability—a gap this research tackles [28]

A modified IC method adjusts step size for irradiation changes, achieving 98.84% efficiency and 3.5% less energy loss, excelling in rapid irradiance ramps. Lacking hardware validation and using fixed error thresholds, it struggles with real-world adaptability, a shortcoming this research resolves with intelligent V_{ref} prediction and tuning [29]. A hybrid P&O with Fuzzy Logic Control uses fuzzy rules for dynamic duty cycle adjustment, achieving 99.91% efficiency and <0.15 W oscillations under rapid irradiance shifts (35 W/m²/s), robust to noise without extra hardware. However, 25-rule tuning increases complexity, unsuitable for resource-limited systems, and boost converter validation limits applicability, reflecting hybrid MPPT challenges [30].

2.2. Hybrid MPPT Methods (Intelligent + Classical)

A hybrid P&O and Fuzzy Logic Control (FLC) approach enhances standalone PV energy harvesting, achieving 24% more gain than P&O, reducing oscillations, and validated via simulations and Arduino. FLC increases computational complexity, limiting low-cost use, and buck converter restriction and no ANN comparison reduce applicability, gaps this research addresses [22]. A P&O-Sliding Mode Control (SMC) hybrid for MPPT and battery SOC management in dual buck-boost systems reduces oscillations and enhances robustness under dynamic conditions. SMC's adaptive tracking ensures stability, but complex design and tuning hinder cost-sensitive adoption, a limitation this research tackles [23].

An Adaptive Neuro-Fuzzy Inference System (ANFIS) for MPPT achieves 99.11% efficiency vs. 99.06% for FLC, reducing switching losses and adapting to nonlinearities in boost converters and grid inverters. High computational load and complex training challenge embedded system use, gaps addressed by this research [24]. A hybrid Feed-Forward Neural Network (FFNN) for V_{ref} prediction with Generalized Super-Twisting Sliding Mode Control achieves 99.11% efficiency and 0.003 s tracking, outperforming backstepping. Extensive FFNN training, tuning complexity, and lack of experimental validation limit feasibility, shortcomings this research resolves [25].

2.3. Metaheuristic-Tuned PID/FOPID Controllers

A variable-step Incremental Conductance (IC) MPPT with Genetic Algorithm (GA)-tuned PID controller for standalone PV systems achieves 46.8% faster convergence, 94.77% ripple reduction, and 49.2% overshoot minimization vs. P&O, suitable for 8-bit microcontrollers. Offline tuning and lack of intelligent V_{ref} prediction limit adaptability under fast-changing conditions, gaps this research addresses [19]. A Particle Swarm Optimization (PSO)-tuned PID controller with IC MPPT for a PV boost converter, guided by ITSE, achieves faster settling and lower overshoot under dynamic disturbances. Static IC V_{ref} and PSO's computational load limit real-time, low-cost deployment, shortcomings this research tackles with ANN-based V_{ref} [20].

A dp/dv-based Fractional Order PID (FOPID) controller, tuned by Aquila Optimizer (AO) with ITAE, outperforms PID, P&O, and MFO-tuned FOPID under dynamic conditions. Fractional orders improve adaptability, but lacking V_{ref} prediction and AO's computational demands limit real-time use, gaps this research resolves [21]. A Dynamic Variable Step P&O (DVPO) with Hunter-Prey Optimizer (HPO)-tuned Fractional PI (FPI) controller for MPPT achieves 0.063–0.087 s convergence and higher power output vs. PSO, GWO, CSA. Fractional calculus enhances nonlinearity response, but no intelligent V_{ref} and HPO complexity challenge real-time implementation, limitations this research addresses [18].

2.4. ANN-based or Adaptive V_{ref} Generation Methods

A hybrid MPPT integrates Feed-Forward Neural Network (FFNN) V_{ref} prediction with Global Sliding Mode Controller, achieving 99.8% accuracy and <0.003 s settling, eliminating chattering. FFNN adapts to environmental variations, but offline training, high complexity, and no

experimental validation limit low-resource applicability, gaps this research addresses [25]. A hybrid MPPT combines Feedforward Neural Network (FNN) V_{ref} prediction with adaptive FOPID, achieving 25.4% higher accuracy and 11.3% faster response than FOPID, with reduced oscillations. Offline tuning, limited validation under partial shading, and ANN overhead limit scalability, shortcomings this research resolves [26].

A hybrid MPPT uses ANFIS for V_{mpp} prediction with PSO-tuned FOPID/PID controllers, reducing overshoot and settling time under variable conditions. ANFIS enhances V_{ref} accuracy, but offline training, PSO complexity, and static V_{ref} in some conditions limit real-time use, gaps this research tackles [6]. A hybrid MPPT employs Cuckoo Search (CS) for V_{ref} generation with Super-Twisting Sliding Mode Control, achieving 100% efficiency and 0.27–0.58 s convergence under partial shading. CS explores MPP, but lacks real-time sensing and predictive intelligence, limiting dynamic adaptability, a gap this research addresses [17]. An AO-tuned FOPID MPPT controller outperforms MFO, PID, and P&O under variable conditions. Lacking adaptive V_{ref} and hybrid intelligence, with high computational complexity, it struggles with rapid changes, limitations this research resolves [18].

2.5 Summary

This chapter investigates classical, hybrid, and intelligent MPPT techniques for photovoltaic systems, highlighting trade-offs between simplicity, efficiency, and adaptability. While intelligent and metaheuristic methods offer high accuracy and fast tracking, they often face real-time implementation challenges due to complexity and computational demands. To address these limitations, the proposed method introduces an adaptive, low-complexity MPPT approach with intelligent V_{ref} prediction, ensuring efficient and robust performance under dynamic conditions.

Chapter 3: System's Control Scheme and Methodology

3.1 Standalone PV-Battery Architecture

The proposed standalone PV system, shown in Figure 1, integrates a PV array, DC–DC buck converter, and battery bank with a neuro-adaptive control loop for MPPT. A Feedforward Neural Network (FNN) predicts V_{ref} using irradiance and temperature data, guiding a Fractional Order PID (FOPID) controller. The error between measured PV voltage (V_{mpp}) and V_{ref} drives the FOPID to adjust the buck converter's PWM duty cycle, optimizing MPPT under dynamic conditions. Metaheuristic optimization tunes FOPID parameters via ITAE, ensuring fast convergence and stability. The battery bank enables single-stage energy storage, enhancing efficiency and simplicity for future real-time deployment.

3.2 MPPT Control Strategy

The system combines ANN, PID/FOPID controllers, and metaheuristic tuning for adaptive MPPT under varying conditions.

3.2.1 Role of ANN in V_{ref} Prediction

A Feedforward Neural Network (FNN) estimates V_{ref} for MPPT using real-time irradiance and temperature inputs. Trained offline on diverse data, the FNN maps inputs to V_{ref}, guiding the DC–DC converter to maximize power extraction.

3.2.2 Controller Design. PID and FOPID

The error between PV voltage and ANN-predicted V_{ref} is processed by PID or FOPID controllers. PID uses standard gains (K_p, K_i, K_d), while FOPID adds fractional orders (λ, μ) for nonlinear systems. Both adjust the PWM duty cycle to match V_{ref}.

3.2.3 ITAE as Optimization Objective

PID and FOPID parameters are tuned to minimize the Integral of Time-weighted Absolute Error (ITAE).

$$\text{ITAE} = \int_0^T t.|e(t)|dt \tag{3.1}$$

where e(t) is the error between V_{ref} and PV voltage. ITAE penalizes persistent errors, ensuring fast, stable response.

3.3 Metaheuristic Tuning and Comparison Workflow

3.3.1 Optimization Process

Metaheuristic algorithms tune PID (K_p, K_i, K_d) and FOPID (K_p, K_i, K_d, λ, μ) parameters to minimize ITAE, optimizing MPPT error and response. Algorithms include PSO, GA, DE, ABC, CS, ACO, WOA, and GWO, operating independently in simulations.

3.3.2 Fair Comparison Setup

Both controllers use the same ANN V_{ref}, environmental conditions, and load profiles. Metrics (efficiency, overshoot, settling time, ripple, energy loss) ensure fair evaluation of controller and tuning performance.

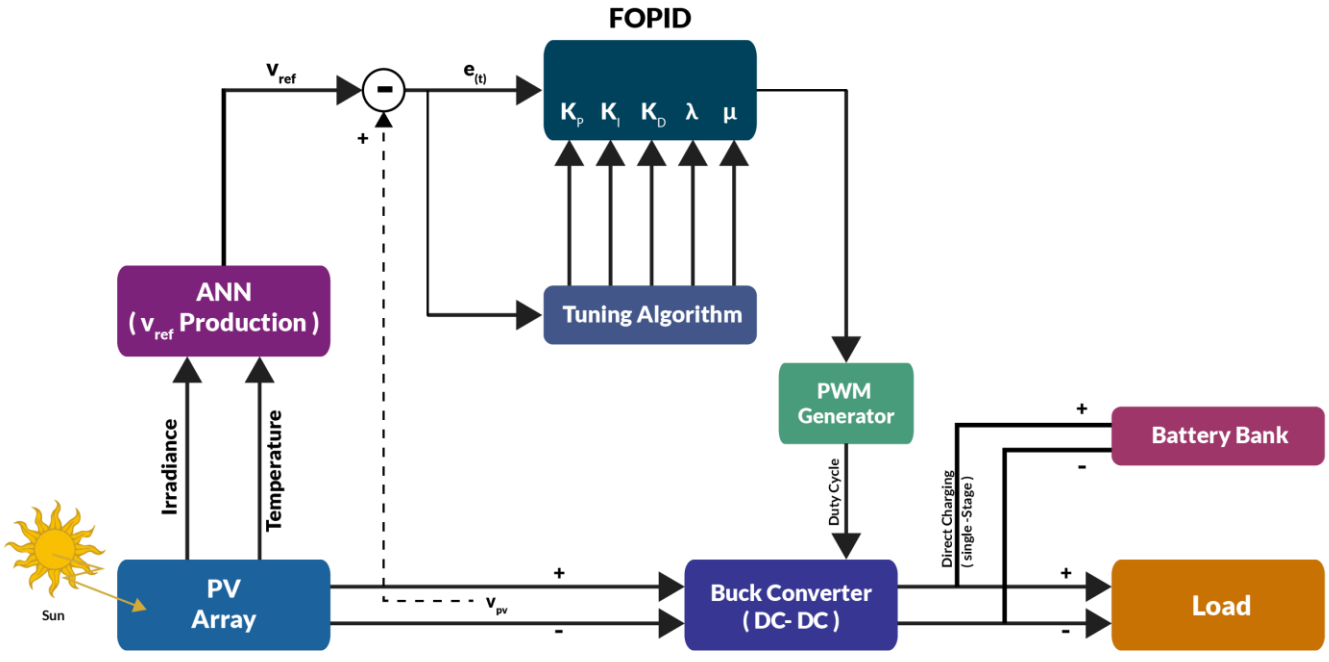

Figure 3.1. Schematic diagram of the Proposed system

3.3.3 Overall System Flow Diagram

Figure 3.1 shows the workflow. Sensors feed irradiance and temperature to the ANN for V_{ref} prediction. The error between V_{ref} and PV voltage drives the PID/FOPID controller, adjusting the PWM duty cycle. Metaheuristic algorithms optimize parameters via ITAE, achieving efficient MPPT.

3.4 Summary

This chapter presents a standalone PV-battery system that employs a Feedforward Neural Network (FNN) for real-time reference voltage (V_{ref}) prediction and a PID/FOPID controller for MPPT, with metaheuristic tuning based on the ITAE criterion. The FNN enhances adaptability to irradiance and temperature changes, while the optimized controllers ensure fast convergence, low error, and stable performance. A fair comparison framework evaluates multiple metaheuristic algorithms across identical conditions, validating the system's robustness, efficiency, and suitability for real-time deployment.

Chapter 4: Implementation

4.1 Photovoltaic System Model

4.1.1 Overview of PV Array and Solar Cell

A photovoltaic (PV) array comprises interconnected solar cells converting irradiance to electricity via p–n junctions. The single-diode model is used for its balance of accuracy and simplicity.

4.1.2 Equivalent Circuit Model and Governing Equations

The single-diode model (Figure 4.1) includes a current source, diode, series resistance R_s, and shunt resistance R_{sh}. The PV cell output current is.

$$I_{pv} = N_p I_{ph} - I_D - I_{sh} \tag{4.1}$$

Here, N_p is parallel cells, I_{ph} is photo-generated current, is diode current, and I_{sh} is shunt current. Photo-generated current is.

$$I_{Ph} = \left(\frac{S}{S_{ref}}\right) \cdot I_{sC} + K_i\left(T - T_{ref}\right) \tag{4.2}$$

With S as irradiance, $S_{ref} = 1000\, W/m^2$, I_{sc} as short-circuit current, K_i as temperature coefficient, T as cell temperature, and $T_{ref} = 25^{\circ}C$. Diode current follows.

$$I_D = I_{rs} N_p [\exp\left(\frac{q\left(V_{pv} + I_{pv} R_s\right)}{nKN_s T}\right) - 1] \tag{4.3}$$

Where, I_{rs} is reverse saturation current, q is electron charge, V_{pv} is output voltage, n is ideality factor, K is Boltzmann's constant, and N_s is series cells. Reverse saturation current is.

$$I_{rs} = I_{rn} \left(\frac{T}{T_{ref}}\right)^3 . \exp\left[\frac{E}{nK}\left(\frac{1}{T_{ref}} - \frac{1}{T}\right)\right] \tag{4.4}$$

With I_{rn} as nominal reverse current and E as bandgap energy. Shunt current is.

$$I_{sh} = \frac{V_{pv} + I_{pv}R_s}{R_{sh}} \quad (4.5)$$

4.1.3 PV Module Selection and Parameters

The Kyocera Solar KD320GX-LPB PV module, implemented in MATLAB/Simulink, uses the above equations with parameters from datasheet (Table 4.1). The single-diode model is shown in Figure 4.1

Table 4.1. Model data and parameters of the PV module (Kyocera Solar KD320GX-LPB).

Module Data and Parameters	Symbols	Values	Units
Maximum power	P_{max}	320.399	Watt, W
Open Circuit Voltage	V_{oc}	49.5	Volt, V
Short circuit Current	I_{sc}	8.6	Ampere, A
Maximum Power Point Voltage	V_{mpp}	40.1	Volt, V
Maximum Power Point Current	I_{mpp}	7.99	Ampere, A
Temperature coefficient of V_{oc}	β_{Voc}	-0.3624	Percentage/deg.celsius, %/°C
Temperature coefficient of I_{oc}	α_{Isc}	0.071	Percentage/deg.celsius, %/°C
Cells per Module	N_{cell}	80	
Light generated Current	I_L	8.6153	Ampere, A
Diode Saturation Current	I_s	3.2022×10^{-10}	Ampere, A
Diode Ideality Factor	n	1.0039	
Shunt Resistance	R_{sh}	233.3987	Ohm, Ω
Series Resistance	R_s	0.41435	Ohm, Ω

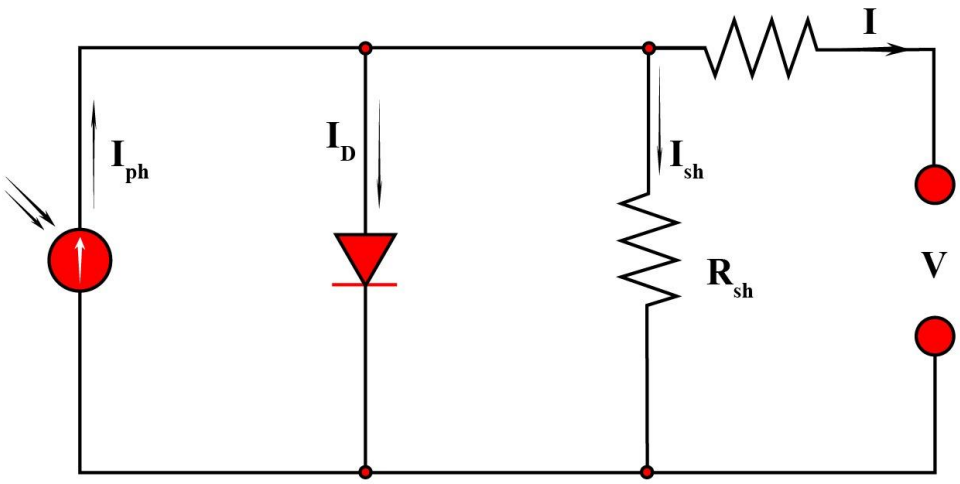

Figure 4.1. Equivalent circuit of a solar cell (single diode model of a PV module).

4.2 Battery Model and Storage Configuration

4.2.1 Mathematical Model of the Battery

The battery model, based on Tremblay and Dessaint's Shepherd equation [31], is used for dynamic simulations.

$$V_{batt} = E_0 - R_i - K\frac{Q}{Q - \int i\,dt} + A.exp\left(-B.\int i\,dt\right) \tag{4.6}$$

where E_0 is constant voltage, R is internal resistance, K is polarization resistance, and A, B define the exponential zone, and $\int i\,dt$ is battery charge (Ah). It models nonlinearities and SOC-driven voltage for robust simulations.

4.2.2 Battery Block Parameters and Implementation

A lead-acid battery, selected for its availability and suitability, is implemented in MATLAB/Simulink with parameters for accurate charge/discharge simulation (Table 4.2).

Table 4.2. Technical specifications of the battery model.

Nominal and Discharge Parameters	Values	Units
Nominal Voltage, V_{nom}	12	Volt, V
Rated Capacity, C_{rated}	160	Ampere-hour, Ah
Initial State of Charge, SOC_{init}	55	Percentage, %
Maximum Capacity, C_{max}	166.6667	Ampere-hour, Ah
Cut-off Voltage, V_{cutoff}	18	Volt, V
Fully Charged Voltage, $V_{fullycharged}$	26.1316	Volt, V
Nominal Discharged Current, $I_{discharged}$	32	Ampere, A
Internal Resistance, $R_{internal}$	0.0015	Ohm, Ω
Capacity at Nominal Voltage, C_{nom}	49.6444	Ampere-hour, Ah
Exponential Zone (Voltage, Capacity), (V_{exp},C_{exp})	(24.4342,0.5.33333)	(Ampere-hour,Volt), (Ah,V)

4.2.3 Selection of Output Voltage and Integration with Buck Converter

The buck converter reduces PV voltage to 12V for efficient PV-battery energy transfer, matching the 12V lead-acid battery. P–V characteristics (Figure 4.2) under varying irradiance (100–1000W/m²) and temperature (–25 to 50°C) [32] show $V_{MPP(min)} \approx$ 39V. Per constraint $V_{out} < V_{MPP(min)}$ [32], 12V enables single-stage charging, enhancing efficiency and simplicity.

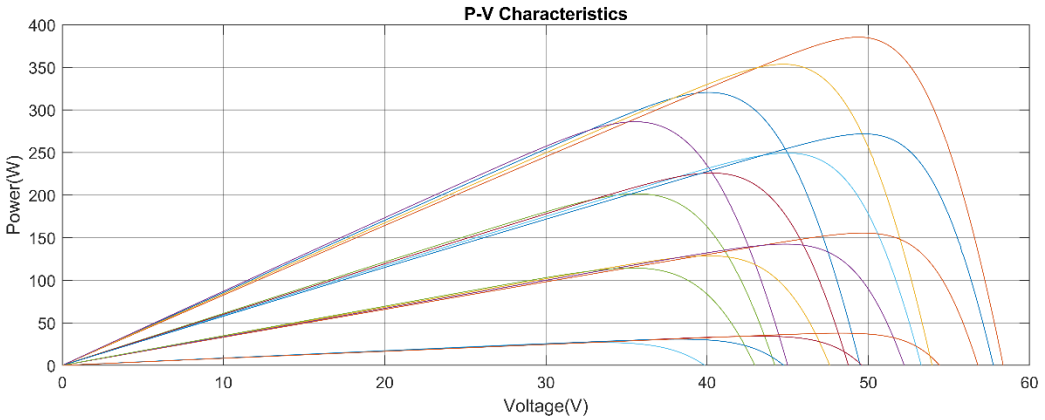

Figure 4.2. P-V characteristics curve for the PV module under normal conditions.

4.3 Buck Converter Design

The buck converter steps down PV voltage (~40.1 V) to 12 V for battery charging in the standalone PV system. Its design, modeling, and component selection are detailed below.

4.3.1 Working Principle of Buck Converter

A buck converter uses switching and storage elements (inductor, capacitor) to reduce ~40.1 V to 12 V, with duty cycle.

$$D = \frac{V_{out}}{V_{in}} \tag{4.7}$$

Operating at 25 kHz, the MOSFET switch stores energy in the inductor during ON state and releases it to the load during OFF state, maintaining stable output.

4.3.2 Simulink Implementation

The buck converter, modeled in MATLAB/Simulink for performance evaluation, includes PV source, MOSFET switch, diode, inductor, input capacitor, and resistive load (battery). Figure 4.3 shows the model. The input capacitor suppresses voltage ripples; no output capacitor is needed due to battery capacitance, simplifying design without performance loss [32]

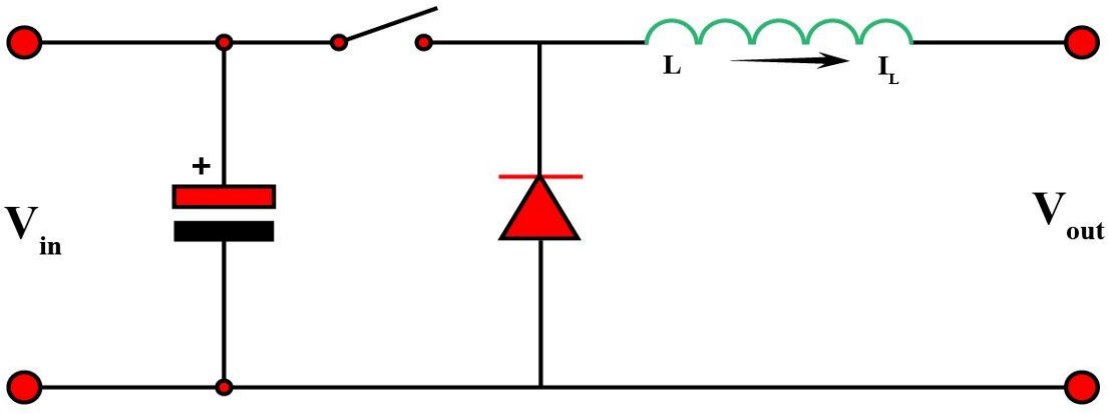

Figure 4.3. Schematic diagram of a dc-dc buck converter.

4.3.3 Component Selection and Design

Passive components ensure low ripple and continuous conduction mode (CCM) using buck converter equations [33-34]

Inductor (L) Selection

The inductor manages current ripple for CCM, calculated as.

$$L = \frac{V_{out} \times (V_{in} - V_{out})}{f_{sw} \times \Delta I \times V_{in}} \tag{4.8}$$

With $V_{in} \approx 40.1\,V$, $V_{out} = 12\,V$, $f_{sw} = 25\,kHz$, ΔI = 0.799A (10% of I_{out} =7.99 A), $L = 2.889 \times 10^{-4}\,H$. Inductor series resistance R_L = 0.9 Ω.

Input Capacitor (C_{in}) Selection

The input capacitor filters transients, calculated as.

$$C_{in} = \frac{\Delta I_L}{8 \times f_{sw} \times \Delta V_{in}} \tag{4.9}$$

stabilizing output during load changes. Where ΔI_L = Inductor current ripple, ΔV_o = Allowed output voltage ripple (1% of output voltage).

Selected Component Values

Component values for 25 kHz operation are listed in Table 4.3

Table 4.3. Model parameters of the buck converter.

Converter Parameters	Values	Units
Input Capacitor, C_{in}	2.7791×10^{-5}	Farad(F)
Inductor, L	2.889×10^{-4}	Henry(H)
Inductor Resistance, R_L	0.9	Ohm(Ω)
Load Resistance, R_{Load}	1.797	Ohm(Ω)

4.4 Neural Network Modeling for Reference Voltage Prediction

The FNN modeling, adapted from [26], uses a dataset generated by varying temperature and irradiance for PV module characteristics.

4.4.1. Selection of Neural Network Type

A 4-layer Feedforward Neural Network (FNN) estimates V_{ref} for MPPT, chosen for its ability to map nonlinear relationships. With three hidden layers and one output layer, it models PV output dependency on irradiance and temperature, providing accurate voltage predictions.

4.4.2. Selection of Input and Output (Training Dataset)

The FNN inputs are irradiance (G, W/m²) and temperature (T, °C), affecting PV performance, with output V_{ref} for MPPT control. The dataset varies T (2–60°C, 2°C steps) and G (400–1000 W/m², 1 W/m² steps), covering typical PV operation. A 1% loss is applied to V_{mpp} to reflect real-world inefficiencies.

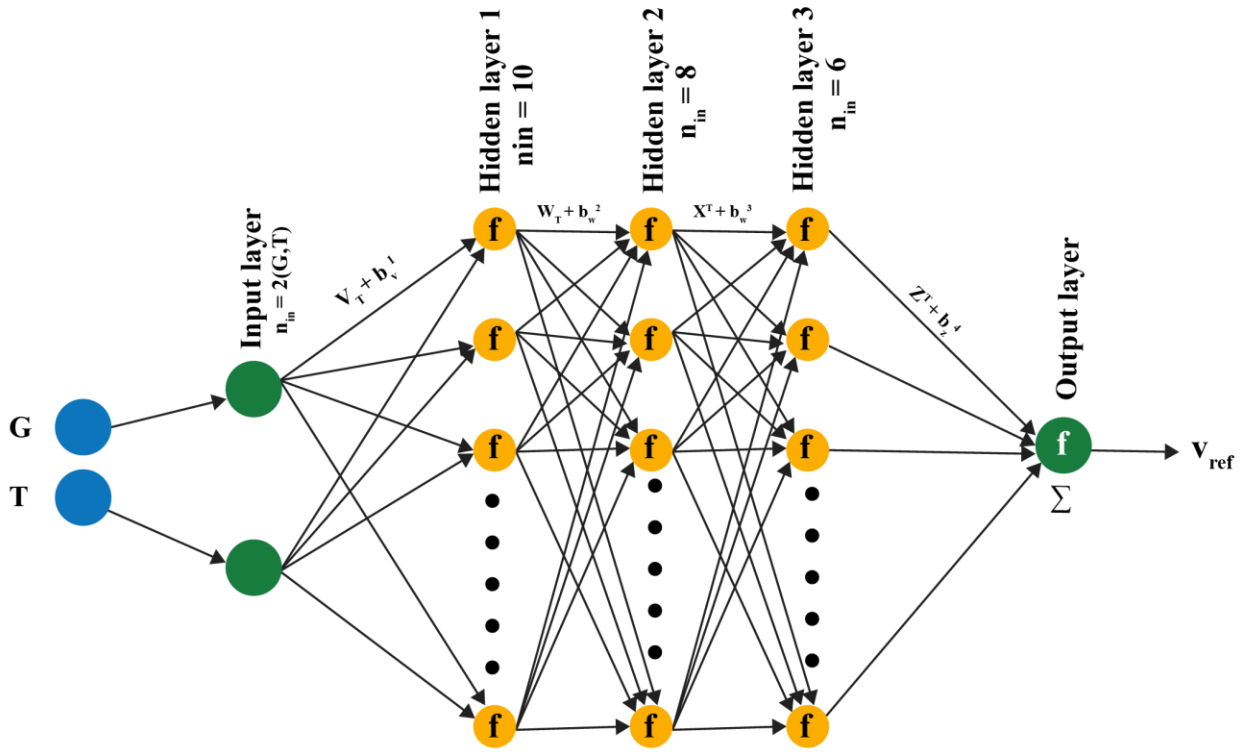

Figure 4.4. Four-Layer FNN block for V_{ref} generation.

4.4.3. FNN Network Architecture

The 4-layer FNN has two input neurons (irradiance, temperature), three hidden layers (10, 8, 6 neurons) with tanh sigmoid activation, and one output neuron (V_{ref}) with linear activation. This structure, shown in Figure 4.4., provides sufficient capacity for voltage prediction. Weight and bias dimensions are in Table 4.4.

Table 4.4. Dimensions of Weight Matrices and Bias Vectors.

Layer Connection	Weight Matrix	Size	Bias Vector	Size
Input Layer ↓ Hidden Layer 1	V^T	$n_1 \times 2$	b_v^1	$n_1 \times 1$
Hidden Layer 1 ↓ Hidden Layer 2	W^T	$n_2 \times n_1$	b_w^2	$n_2 \times 1$
Hidden Layer 2 ↓ Hidden Layer 3	x^T	$n_3 \times n_2$	b_x^3	$n_3 \times 1$
Hidden Layer 3 ↓ Output Layer	Z^T	$n_3 \times 1$	b_z^4	1×1

4.4.4 Transfer Function of FNN

Hidden layers use the hyperbolic tangent sigmoid function.

$$f(a) = tanh(a) = \frac{e^a - e^{-a}}{e^a + e^{-a}} \tag{4.10}$$

enabling nonlinear modeling and training via backpropagation.

4.4.5 Mathematical Modeling of the Four-Layer FNN

Input vector. $$p = \begin{bmatrix} I \\ T \end{bmatrix}$$

This vector represents the input features to the network. irradiance(I) and temperature(T).

First Hidden Layer: Combines inputs with bias.

$$\boldsymbol{a^{(1)} = V^T p + b_{v1}} \tag{4.11}$$

Activation function. $y^{(1)} = tanh\left(a^{(1)}\right)$, with $V^T \in \mathbb{R}^{10\times2}$ and $b_{v1} \in \mathbb{R}^{10\times1}$.

Second Hidden Layer:

$$a^{(2)} = W^T y^{(1)} + b_{w2} \tag{4.12}$$

Activation function. $y^{(2)} = tanh\left(a^{(2)}\right)$, with $W^T \in \mathbb{R}^{8\times10}$ *and* $b_{w2} \in \mathbb{R}^{8\times1}$.

Third Hidden Layer:

$$a^{(3)} = X^T y^{(2)} + b_{x3} \tag{4.13}$$

Activation function. $y^{(3)} = tanh\left(a^{(3)}\right)$, with $X^T \in \mathbb{R}^{6\times8}$ and $b_{x3} \in \mathbb{R}^{6\times1}$.

Output Layer: with $Z^T \in \mathbb{R}^{1\times6}$ and $b_{z4} \in \mathbb{R}^{1\times1}$.

$$V_{ref} = Z^T y^{(3)} + b_{z4} \tag{4.14}$$

Compact Representation:

$$V_{ref} = Z^T tanh(X^T tanh(W^T tanh(V^T p + b_{v1}) + b_{w2}) + b_{x3}) + b_{z4} \tag{4.15}$$

4.4.6 Cost Function

The mean squared error (MSE) cost function trains the FNN.

$$J = \frac{1}{2}\left(t - V_{ref}\right)^2 \tag{4.16}$$

minimizing prediction errors, aiding backpropagation, where t is the target voltage.

4.4.7 Validation of Trained Model

FNN performance is validated via regression plot (Figure 4.5.), error histogram (Figure 4.6), and performance plot (Figure 4.7.). The regression plot shows strong correlation (R ≈ 1). The error histogram indicates minimal errors centered at zero. The performance plot shows MSE convergence to 8.2411×10^{-4} after 124 epochs using Levenberg–Marquardt, confirming accurate and stable V_{ref} prediction for MPPT.

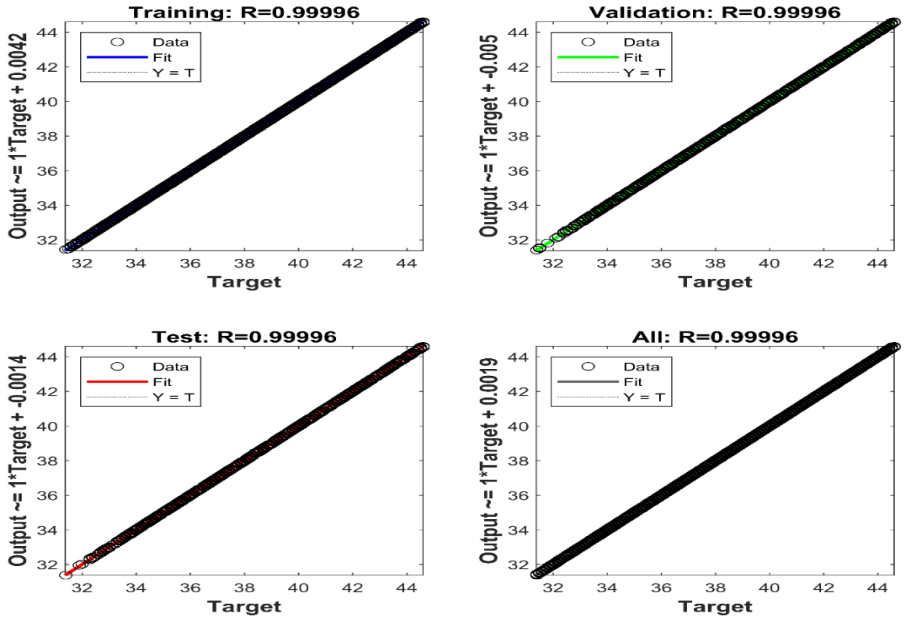

Figure 4.5. The regression plots during the estimation of V_{ref} .

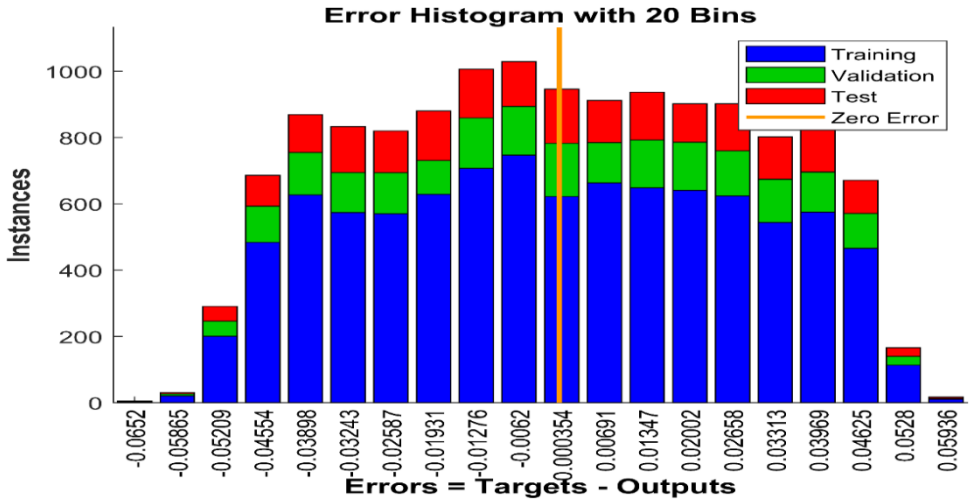

Figure 4.6. The error histogram during the estimation of V_{ref}.

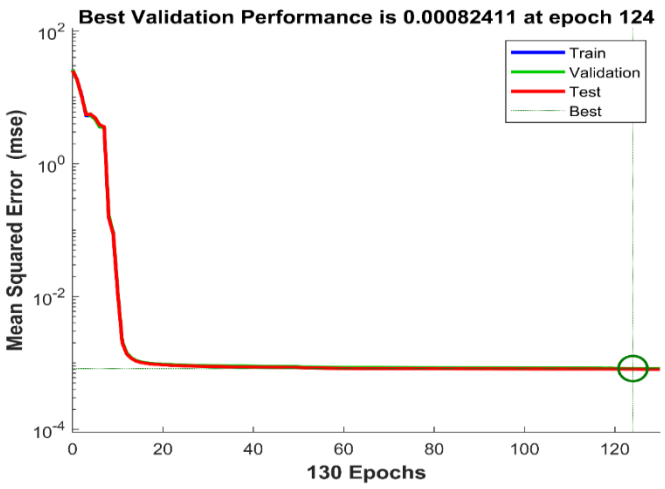

Figure 4.7. Mean square error convergence during the V_{ref} estimation.

4.5 Overview of Optimization Algorithms Used

This section overviews eight optimization algorithms (PSO, GA, ABC, DE, CS, GWO, ACO, WOA) used to tune PID and FOPID controllers for MPPT in a standalone PV-battery system. Each algorithm's mechanism, mathematical formulation, and simulation parameters are detailed for reproducibility.

4.5.1 Particle Swarm Optimization (PSO) [35-36]

PSO updates a swarm of 15 particles' velocities and positions based on personal and global best solutions to optimize controller parameters.

$$v_i{}^{t+1} = w \cdot v_i{}^{t} + c_1 \cdot r_1 \cdot (p_i{}^{best} - x_i{}^{t}) + c_2 \cdot r_2 \cdot (g_b{}^{best} - x_i{}^{t}) \quad (4.17)$$

$$x_i{}^{t+1} = x_i{}^{t} + v_i{}^{t+1} \quad (4.18)$$

Here, $v_i{}^{t}$ and $x_i{}^{t}$ are velocity and position, w is inertia weight, c_1,c_2 are acceleration coefficients, r_1 and r_2 are random numbers in [0,1], $p_i{}^{best}$ and $g_b{}^{best}$ are best positions.

Parameter values used: Number of particles = 15, inertia weight w varies linearly from 1 (max) to 0.1 (min), cognitive coefficient c_1=2, social coefficient c_2=2.

4.5.2 Artificial Bee Colony (ABC) [37-38]

ABC uses 30 bees (15 employed, 15 onlooker) to explore and select solutions (food sources). Employed bees generate new solutions.

$$v_{ij} = x_{ij} + \phi_{ij}(x_{ij} - x_{kj}) \tag{4.19}$$

Here, v_{ij} is the new solution, x_{ij} is the current solution, x_{kj} is a randomly selected neighbor solution, and ϕ_{ij} is a random number in [-1, 1]. Onlooker bees select solutions with probability.

$$p_i = \frac{fit_i}{\sum_{n=1}^{SN} fit_n} \tag{4.20}$$

Where fit_i is the fitness of solution, and SN is food source count. Scout bees replace abandoned solutions.

Parameter values used: Number of employed bees = 15, number of onlooker bees = 15 (i.e., colony size = 30), abandonment limit = 10.

4.5.3 Genetic Algorithm (GA) [39-40]

GA evolves a population of 15 solutions using selection, crossover, and mutation. Selection probability.

$$p_i = \frac{f_i}{\sum_{j=1}^{N} f_j} \tag{4.21}$$

where p_i is the probability of selecting the i^{th} individual, and f_i is its fitness. Crossover creates offspring.

$$offspring_1 = parent_1[1.k] + parent_2[k + 1.n] \tag{4.22}$$

$$offspring_2 = parent_2[1.k] + parent_1[k + 1.n] \tag{4.23}$$

where k is the crossover point. Mutation adds perturbation.

$$x_i' = x_i + \delta \tag{4.24}$$

Parameter values used: Population size = 15, crossover rate = 0.8, mutation rate = 0.2.

4.5.4 Differential Evolution (DE) [41]

DE generates trial vectors for a population of 15 solutions using mutation and crossover.

$$v_i = x_{r1} + F \cdot (x_{r2} - x_{r3}) \tag{4.25}$$

Here, x_{r1}, x_{r2}, and x_{r3} are distinct vectors randomly selected from the population, and F is a scaling factor. Better trial vectors replace original solutions.

Parameter values used: Population size = 15, mutation factor (F) = 0.5, crossover probability (CR) = 0.9.

4.5.5 Cuckoo Search [42]

CS generates new solutions for 15 nests using Lévy flights.

$$x_i{}^{t+1} = x_i{}^{t} + \alpha \cdot Le'vy(\lambda) \tag{4.26}$$

Better solutions replace existing ones; a fraction p_a of worst nests are randomly replaced.

$$x_i = \begin{cases} random(L_b, U_b), & if\ random < p_a \\ x_i, & otherwise \end{cases} \tag{4.27}$$

Parameter values used. Population size (nest count) = 15, maximum iterations = 15, discovery rate of alien eggs p_a=0.25, step size α=1.

4.5.6 Ant Colony Optimization(ACO) [43]

ACO uses 15 ants to construct solutions, with transition probability.

$$p_{ij} = \frac{[\tau_{ij}]^{\alpha} . [\eta_{ij}]^{\beta}}{\sum_{k \in allowed} [\tau_{ik}]^{\alpha} . [\eta_{ik}]^{\beta}} \tag{4.28}$$

Here, τ_{ij} are pheromone and heuristic values, α and β are weights. Pheromone update.

$$\tau_{ij} = (1 - \rho) \cdot \tau_{ij} + \Delta\tau_{ij} \tag{4.29}$$

where ρ is the pheromone evaporation rate, and $\Delta\tau_{ij}$ is the pheromone deposited by ants.

Parameter values used: Number of ants = 15, pheromone evaporation rate ρ=0.5, pheromone influence α=1, heuristic influence β=2.

4.5.7 Grey Wolf Optimization [44]

GWO updates 15 solutions based on alpha, beta, delta wolves.

$$X(t+1) = \frac{X_1 + X_2 + X_3}{3} \tag{4.30}$$

Where. $X_1 = X_\alpha - A_1 \cdot D_\alpha$, $D_\alpha = |C_1 \cdot X_\alpha - X|$, $X_2 = X_\beta - A_2 \cdot D_\beta$,

$D_\alpha = \left|C_1 \cdot X_\beta - X\right|$, with A,C as coefficients.

Parameter values used: Wolf count (population size) = 15. GWO does not require additional control parameters due to its adaptive mechanism.

4.5.8 Whale Optimization Algorithm (WOA) [45]

WOA updates 15 solutions via shrinking encircling.

$$D = |C \cdot X^* - X(t)|, \quad X(t+1) = X^* - A \cdot D \tag{4.31}$$

Where $\vec{A} = 2\vec{a} \cdot \vec{r}_1 - \vec{a}$, $\vec{C} = 2 \cdot \vec{r}_2$, or spiral updating.

$$X(t+1) = D' \cdot e^{bl} \cdot cos(2\pi l) + X^* \tag{4.32}$$

where $\vec{D'} = \left|\vec{X} * -\vec{X}\right|$, Random search occurs if $\left|\vec{A}\right| > 1$.

Parameter values used: Whale count (population size) = 15, spiral constant b=1, convergence parameter aa decreases linearly from 2 to 0.

4.6 PID and FOPID Parameter Tuning for ITAE Minimization

4.6.1 Tuning Framework Overview

PID and FOPID controllers are tuned using eight optimization algorithms (Section 4.5) at 1000 W/m², 25°C, with ITAE.

$$J = \int_0^T \tau \cdot |e(\tau)|\, d\tau \tag{4.33}$$

where e(τ) is the tracking error, penalizing persistent errors for fast settling. PID parameters (K_p, K_i, and K_d) are bounded in [0, 1000], FOPID orders (λ, μ) in [0.01, 0.99], ensuring consistent comparison. Figure 4.8. shows the iterative optimization process using the Whale Optimization Algorithm (WOA) until convergence.

4.6.2 Justification for Tuning Settings

The maximum number of iterations for each optimization algorithm was set to 15. This choice balances computational efficiency and convergence quality. Preliminary tests showed that most algorithms stabilize within 10–12 iterations; thus, 15 iterations ensure sufficient exploration of the parameter space without unnecessary computation or overfitting.

4.6.3 Final Tuned Parameters

Tuned parameters for eight PID and FOPID algorithms are summarized in Table 4.5 and Table 4.6

Table 4.5. Tuned PID Parameters of the optimization algorithms.

Algorithm	Kp	Ki	Kd
PSO	35.89	1000	0.1
ABC	35.68	822.86	0.18
GA	768.86	306.54	615.94
CS	319.37	910.81	885.23
DE	108.99	938.34	0.1
GWO	4.67	888.04	888.04
ACO	133.42	200.08	200.08
WOA	0.1	110.45	0.1

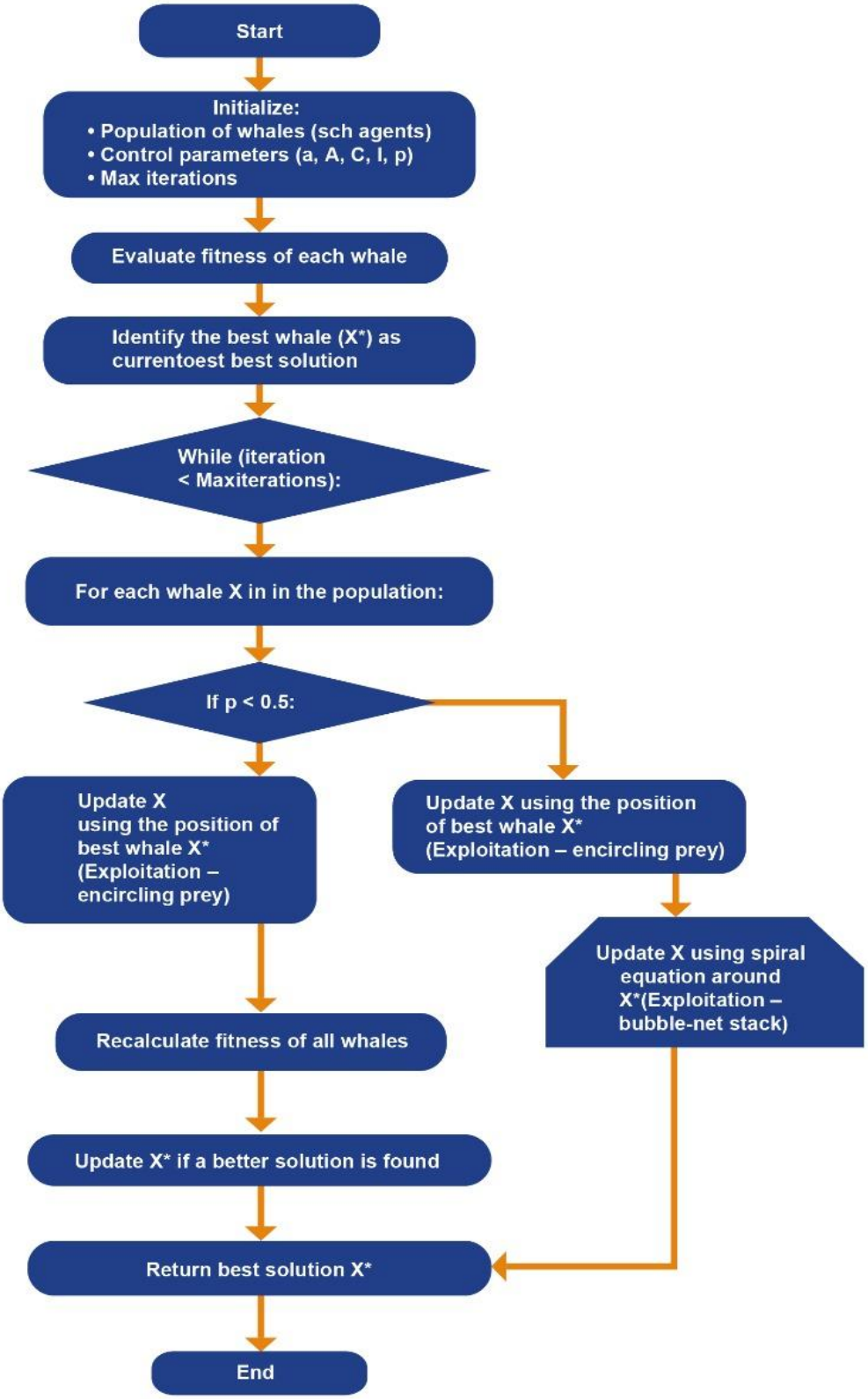

Figure 4.8. Flowchart of optimization algorithms(WOA).

Table 4.6. Tuned FOPID Parameters of the optimization algorithms.

Algorithm	Kp	Ki	Kd	λ	μ
PSO	150.40	800.02	274.66	0.36	0.66
ABC	371.44	78.32	456.41	0.06	0.73
GA	317.26	475.53	599.56	0.75	0.70
CS	457.36	618.14	932.19	0.83	0.89
DE	16.37	688.17	142.90	0.12	0.60
GWO	19.18	199.19	125.85	0.15	0.32
ACO	133.42	200.08	133.42	0.53	0.21
WOA	1.51	4.80	0.10	0.01	0.01

4.6.4 Integration with Simulation.

The parameter sets obtained from the tuning process were applied to all six test scenarios of the standalone PV system.

4.7 Environmental Conditions and Test Cases

4.7.1 Description of Six Test Scenarios

Six test scenarios evaluate the ANN-FOPID MPPT system's robustness under varied conditions, covering gradual and abrupt irradiance/temperature changes.

Case 1**,** Slow Diurnal Irradiance Variation: Irradiance rises from 200 W/m² to 1000 W/m² and back within 0.1 s at 25°C, simulating daily sunlight (Figure 4.9). Tests smooth adaptation.Case 2, Irradiance Drop (Cloud Cover): Irradiance shifts from 1000 W/m² to 600 W/m², 400 W/m², 700 W/m², and back within 0.1 s at 25°C (Figure 4.10). Assesses transient response.Case 3, Slow Diurnal Temperature Variation: Temperature varies from 20°C to 40°C and back at 800 W/m² (Figure 4.11). Evaluates thermal compensation.Case 4, Sudden Temperature Spike (Heatwave): Temperature jumps from 25°C to 45°C, dips to 30°C, then rises to 50°C at 800 W/m² (Figure 4.12). Assesses stability under thermal stress.Case 5, Low Irradiance/Temperature (Morning/Evening): Irradiance rises from 200 W/m² to 500 W/m², temperature from 10°C to 20°C (Figure 4.13, 4.14). Tests low-energy efficiency.Case 6, Extreme High Irradiance/Temperature (Desert/Tropical): Irradiance shifts between 1000–1200 W/m², temperature between 55–60°C (Figure 4.15, 4.16). Tests reliability under high stress.

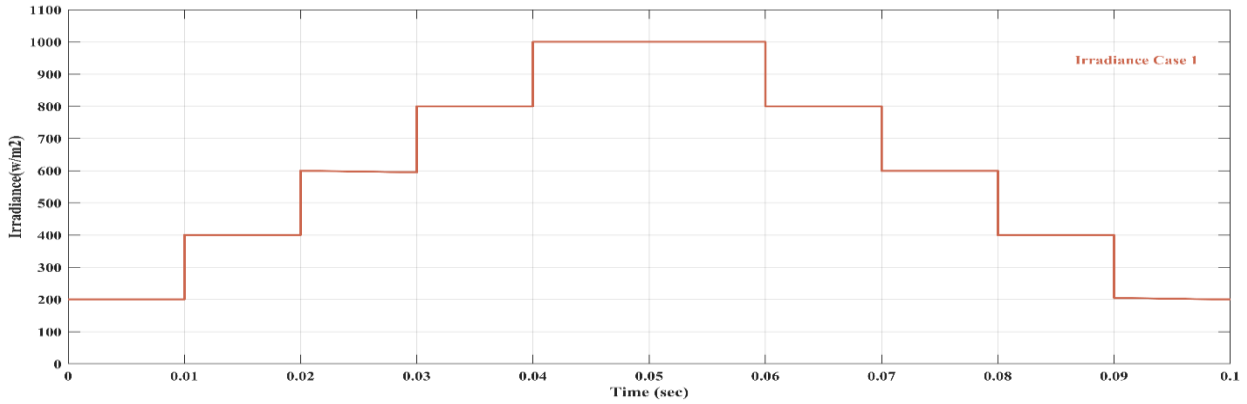

Figure 4.9. Case 1,Slow Diurnal Variation in Irradiance.

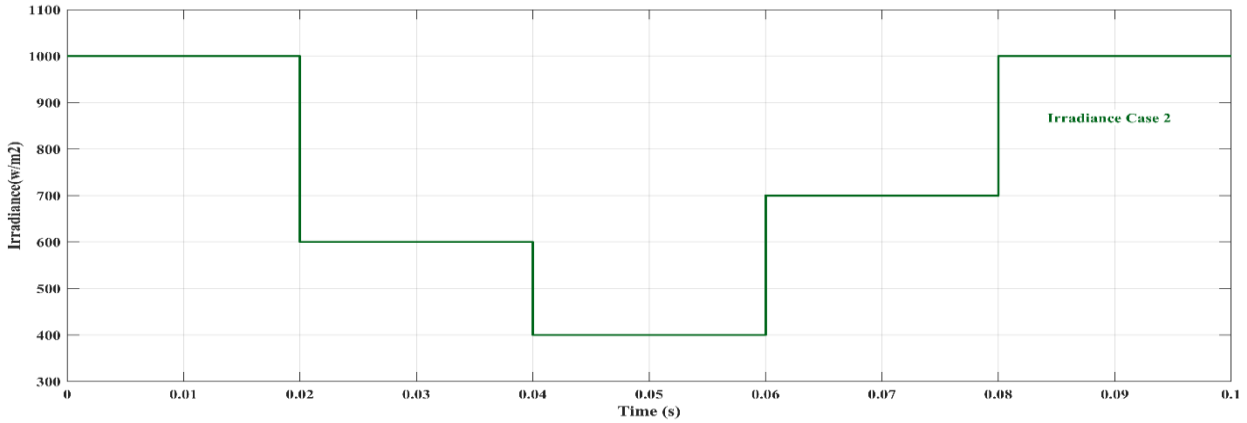

Figure 4.10. Case 2, Irradiance Drop Due to Cloud Cover.

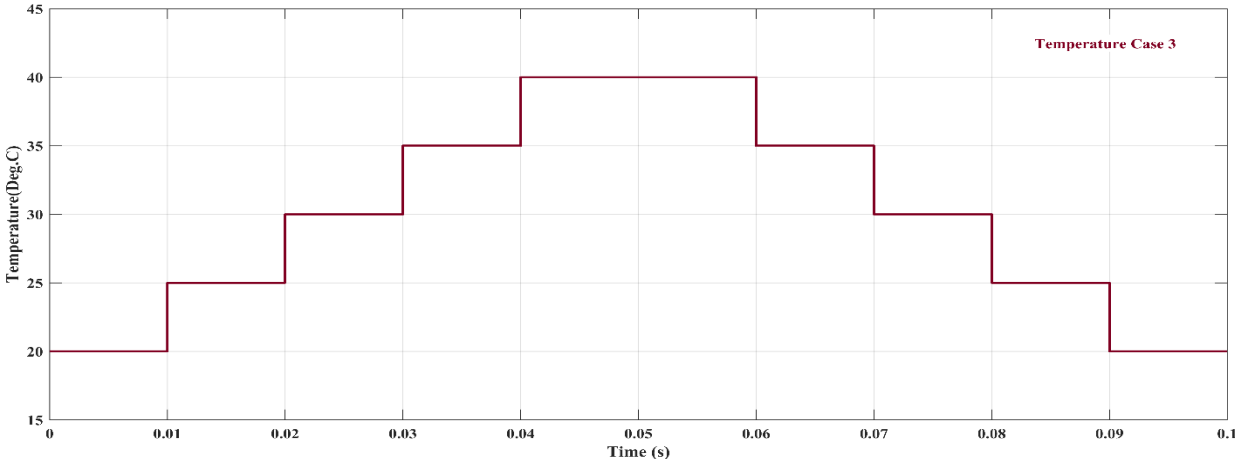

Figure 4.11. Case 3,Slow Diurnal Variation in Temperature.

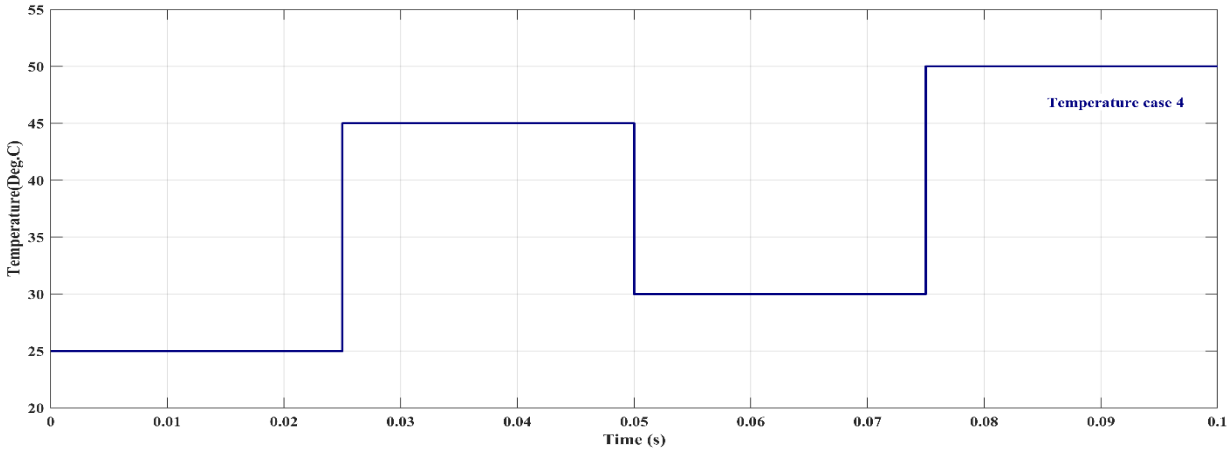

Figure 4.12. Case 4, Sudden Temperature Spike (Heatwave Conditions).

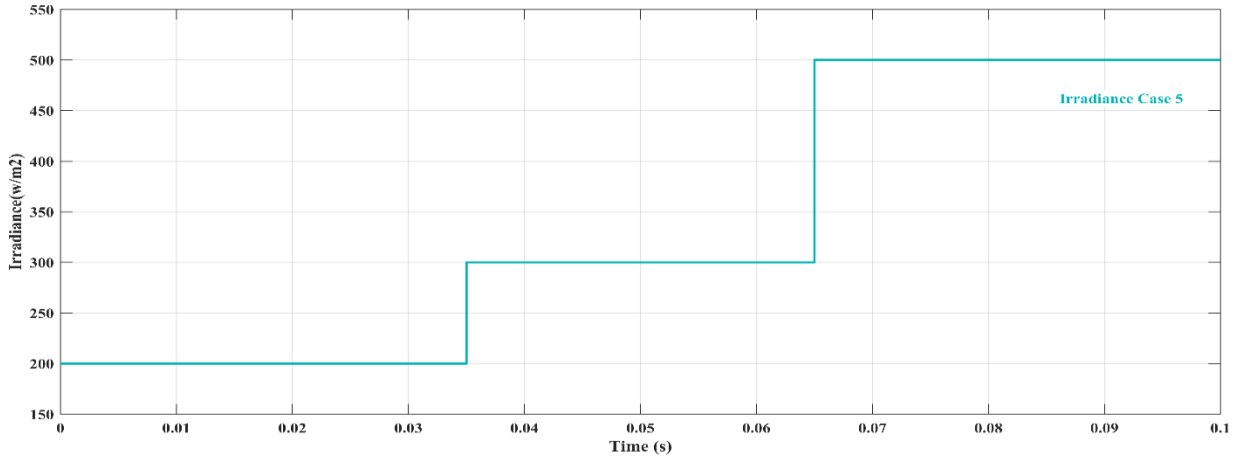

Figure 4.13. Case 5, Low Irradiance (Morning/Evening Conditions).

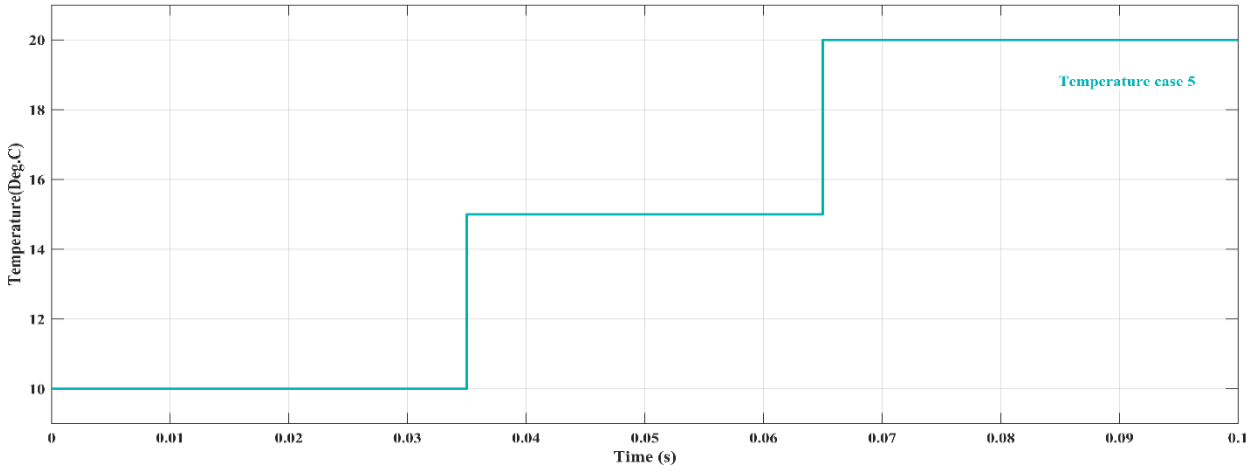

Figure 4.14. Case 5, Low Temperature (Morning/Evening Conditions).

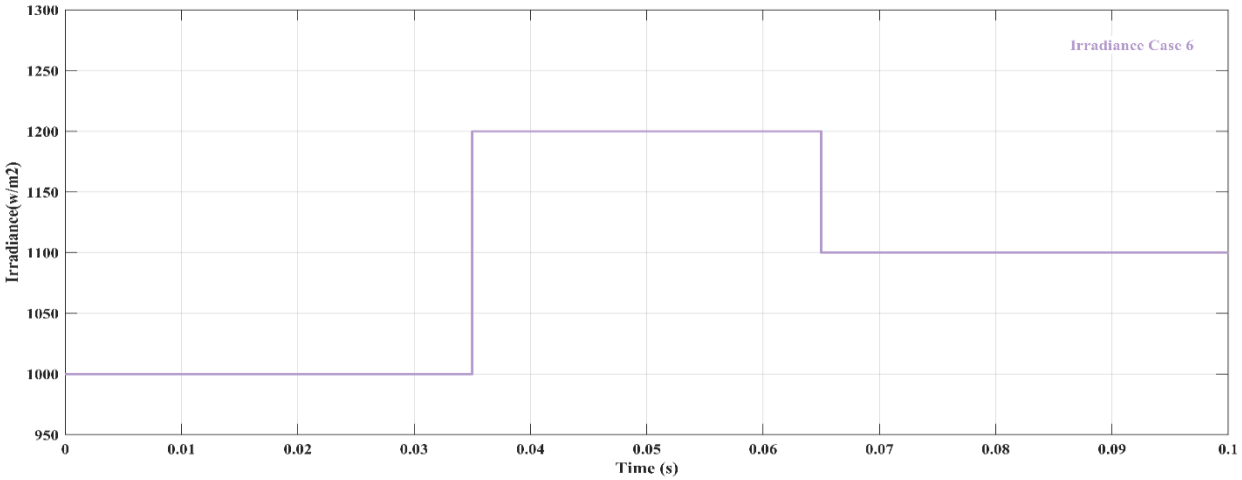

Figure 4.15. Case 6, Extreme High Irradiance (Desert/Tropical Conditions).

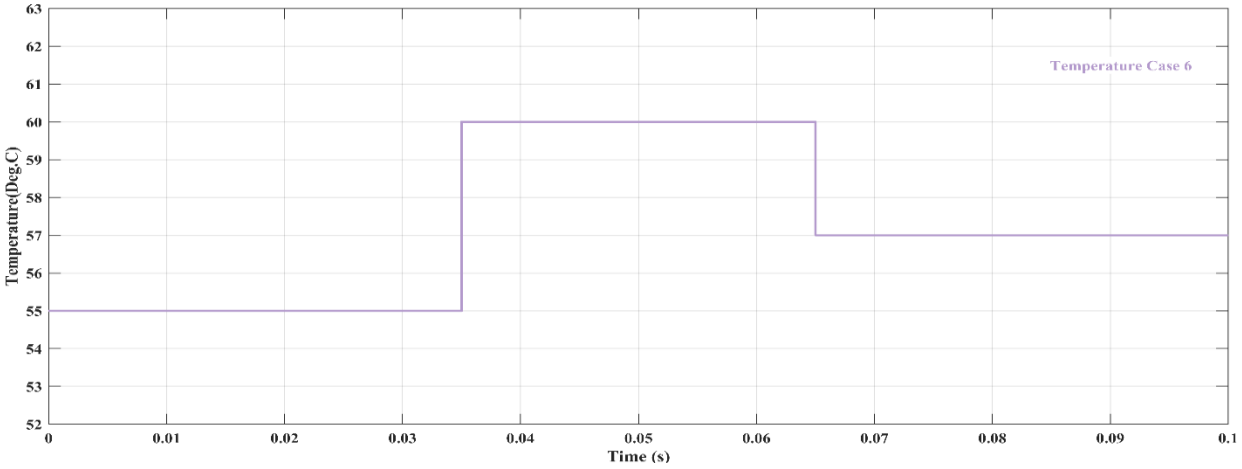

Figure 4.16. Case 6,High Temperature (Desert/Tropical Conditions).

4.7.2 Justification of Selected Cases and Summary Table

The selected environmental test cases were strategically chosen to cover both common and extreme operating conditions encountered by standalone PV-battery systems. These include slow transitions (diurnal patterns), sudden fluctuations (cloud movement or thermal shocks), and boundary cases (low or high irradiance/temperature), ensuring a comprehensive evaluation of system performance. By isolating either irradiance or temperature effects in specific cases, the study ensures clarity in interpreting controller behavior under targeted stressors. Collectively, these cases simulate realistic field conditions, supporting the validity and practical relevance of the proposed control strategy. The corresponding V_{mpp} and P_{mpp} values for these cases are summarized in Table 4.7. These values were extracted from simulation results and used to evaluate six

performance metrics—efficiency, overshoot, ripple, response time, tracking time, and energy loss—for each FOPID tuning algorithm. A summary of the irradiance and temperature profiles for all six cases is presented in Table 4.8 for quick reference.

Table 4.7. Maximum Power Point Voltage (V_{mpp}) and Power (P_{mpp}) for each test case.

Case 1	[Irradiance Temperature]	[200 25]	[400 25]	[600 25]	[800 25]	[1000 25]
	V_{mpp}	39.331	40.0516	40.281	40.2119	40.1
	P_{mpp}	63.1205	128.601	193.649	257.671	320.399
Case 2	[Irradiance Temperature]	[700 25]				
	V_{mpp}	40.2452				
	P_{mpp}	225.808				
Case 3	[Irradiance Temperature]	[800 20]	[800 25]	[800 30]	[800 35]	[800 40]
	V_{mpp}	41.2	40.3	39.3	38.4	37.5
	P_{mpp}	263.0962	257.6692	252.2067	246.7032	241.1613
Case 4	[Irradiance Temperature]	[800 45]	[800 50]			
	V_{mpp}	36.6	35.6			
	P_{mpp}	235.5829	229.9701			
Case 5	[Irradiance Temperature]	[200 10]	[300 15]	[500 20]		
	V_{mpp}	42.3	41.7	41.2		
	P_{mpp}	67.3766	100.0547	164.6745		
Case 6	[Irradiance Temperature]	[1000 55]	[1200 60]	[1100 57]		
	V_{mpp}	34.6	33.5	34.2		
	P_{mpp}	279.0297	323.9396	302.7763		

4.8 Simulink Model

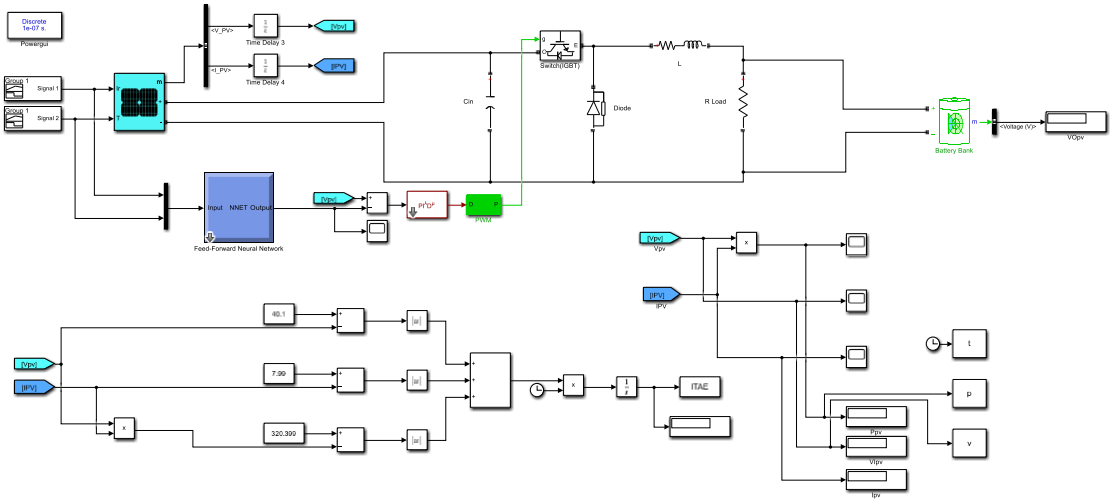

Figure 4.17. Simulink Model of proposed system.

Table 4.8. Irradiance and Temperature case profiles as input.

Cases	Duration (Time in sec.)	Values	
		Irradiance	Temp.
1	0-0.01	200	25
	0.01-0.02	400	25
	0.02-0.03	600	25
	0.03-0.04	800	25
	0.04-0.06	1000	25
	0.06-0.07	800	25
	0.07-0.08	600	25
	0.08-0.09	400	25
	0.09-0.1	200	25
2	0-0.02	1000	25
	0.02-0.04	600	25
	0.04-0.06	400	25
	0.06-0.08	700	25
	0.08-0.1	1000	25
3	0-0.01	800	20
	0.01-0.02	800	25
	0.02-0.03	800	30
	0.03-0.04	800	35
	0.04-0.06	800	40
	0.06-0.07	800	35
	0.07-0.08	800	30
	0.08-0.09	800	25
	0.09-0.1	800	20
4	0-0.025	800	25
	0.025-0.05	800	45
	0.05-0.075	800	30
	0.075-0.1	800	50
5	0-0.035	200	10
	0.035-0.065	300	15
	0.065-0.1	500	20
6	0-0.035	1000	55
	0.035-0.065	1200	60
	0.065-0.1	1100	57

4.9 Summary

This chapter presents a simulation-based performance evaluation of the proposed MPPT system under variable irradiance and temperature conditions using MATLAB/Simulink. It compares PID and FOPID controllers tuned with eight different metaheuristic algorithms, analyzing key performance metrics such as tracking efficiency, overshoot, settling time, and ripple. Results demonstrate that FOPID controllers consistently outperform PID controllers, with the Grey Wolf Optimizer (GWO) delivering the best overall MPPT performance in terms of speed, stability, and minimal energy loss

Chapter 5: Result and Analysis

5.1 Performance Metrics Analysis

This section presents the performance evaluation of PID and FOPID controllers tuned using eight different algorithms across all test cases. The goal is to identify the best-performing PID and FOPID controller individually. Performance comparisons are based on six key metrics. Efficiency, Energy Loss, Tracking Time, Ripple in Voltage, Overshoot, and ITAE. Detailed results are shown in Table 5.1. (PID) and Table 5.2. (FOPID).

5.1.1 PID Metrics Across All Tuning Algorithms and Test Cases

Efficiency: PSO, ABC, and DE consistently achieve the highest efficiency (~99.7% in Case 2). GA, CS, and ACO perform poorly (e.g., GA drops to 96.44% in Case 5).

Ranking: PSO ≈ ABC ≈ DE > GWO > WOA > ACO > GA > CS.

Energy Loss: PSO, ABC, and DE show minimal energy loss (0.04J in Case 1). GA, CS, and ACO have high losses (e.g., CS up to 0.5J in Case 1).

Ranking: PSO ≈ ABC ≈ DE > GWO > WOA > GA ≈ ACO ≈ CS.

Tracking Time: DE achieves the fastest tracking (0.05s in Case 5). GA and CS are the slowest (up to 3.77s for CS in Case 5).

Ranking: DE > PSO ≈ ABC > GWO > WOA > GA ≈ ACO ≈ CS.

Ripple in Voltage: CS, ACO, and GA have the lowest ripple (0.06–0.08% in Case 1). WOA and GWO perform poorly (up to 1.95% for WOA in Case 5).

Ranking: CS > ACO > GA ≈ DE > PSO > ABC > GWO > WOA.

Overshoot: DE has the lowest overshoot (0.3728% in Case 3). WOA and GWO show high overshoot (up to 5.8006% for WOA in Case 5).

Ranking: DE > ACO > PSO ≈ ABC > GA ≈ CS > GWO > WOA.

ITAE: WOA has the lowest ITAE (0.1194 in Case 6). GA, CS, and ACO show high ITAE (up to 0.9867 for CS in Case 5).

Ranking: WOA > GWO > PSO ≈ ABC ≈ DE > GA > ACO > CS.

Table 5.1. PID metrics for all tuning algorithm across all cases.

case			1	2	3	4	5	6
Parameters	Efficiency(%)	PSO	99.48	99.75	99.69	99.72	99.39	99.73
		ABC	99.47	99.75	99.68	99.72	99.39	99.73
		GA	97.26	99.16	98.9	98.99	96.44	99.31
		CS	97.1	99.12	98.85	98.94	96.23	99.28
		DE	99.46	99.74	99.67	99.71	99.38	99.72
		GWO	99.16	99.72	99.62	99.67	98.93	99.75
		ACO	97.16	99.14	98.87	98.96	96.31	99.29
		WOA	98.98	99.72	99.61	99.66	98.68	99.77
	Energy loss(J)	PSO	0.04	0.08	0.07	0.07	0.04	0.08
		ABC	0.04	0.08	0.08	0.07	0.04	0.08
		GA	0.46	0.21	0.27	0.25	0.37	0.21
		CS	0.5	0.22	0.29	0.26	0.39	0.22
		DE	0.04	0.08	0.08	0.07	0.62	0.08
		GWO	0.08	0.09	0.09	0.08	0.09	0.07
		ACO	0.48	0.22	0.28	0.26	0.38	0.21
		WOA	0.1	0.09	0.09	0.09	0.12	0.07
	Tracking Time(s)	PSO	0.79	0.25	0.31	0.28	0.61	0.27
		ABC	0.8	0.25	0.32	0.28	0.61	0.27
		GA	2.74	0.84	1.1	1.01	3.56	0.69
		CS	2.9	0.88	1.15	1.06	3.77	0.72
		DE	0.81	0.26	0.33	0.29	0.05	0.28
		GWO	1.12	0.28	0.38	0.33	1.07	0.25
		ACO	2.84	0.86	1.13	1.04	3.69	0.71
		WOA	1.24	0.28	0.39	0.34	1.32	0.23
	Overshoot(%)	PSO	2.7054	2.7338	0.4032	1.528	4.3463	5.2297
		ABC	2.6159	2.7475	0.4137	1.5109	4.4056	5.2185
		GA	3.084	2.2435	2.6531	1.4963	2.8048	5.0079
		CS	3.162	2.1909	2.6648	1.4918	2.8484	5.0061
		DE	2.5113	2.7046	0.3728	1.5255	4.2719	5.2123
		GWO	2.3411	2.9684	0.4471	1.6037	5.3108	5.1883
		ACO	3.1189	2.2193	0.7985	1.5094	2.8402	4.9771
		WOA	2.4383	3.0823	0.489	1.6366	5.8006	5.245
	Ripple in Voltage(%)	PSO	0.18	0.15	0.15	0.17	0.24	0.19
		ABC	0.21	0.16	0.16	0.2	0.29	0.19
		GA	0.08	0.08	0.08	0.1	0.15	0.12
		CS	0.06	0.07	0.07	0.08	0.07	0.1
		DE	0.1	0.09	0.1	0.1	0.09	0.12
		GWO	0.52	0.39	0.3	0.54	1.57	0.54
		ACO	0.07	0.07	0.07	0.09	0.1	0.11
		WOA	0.75	0.63	0.53	0.82	1.95	0.85
	ITAE	PSO	0.6559	0.4124	0.3564	0.4274	0.965	0.1219
		ABC	0.6556	0.4123	0.3563	0.4273	0.9651	0.1218
		GA	0.6866	0.4231	0.3689	0.4399	0.984	0.128
		CS	0.689	0.424	0.37	0.4409	0.9867	0.1285
		DE	0.6561	0.4126	0.3566	0.4276	0.9648	0.122
		GWO	0.6589	0.4114	0.3556	0.426	0.9707	0.1202
		ACO	0.6881	0.4236	0.3696	0.4405	0.9857	0.1283
		WOA	0.6611	0.4116	0.3559	0.4257	0.9745	0.1194

5.1.2 FOPID Metrics Across All Tuning Algorithms and Test Cases

Efficiency: WOA consistently achieves the highest efficiency across all cases (e.g., 99.79% in Case 2), followed closely by GWO and DE. PSO and ABC perform less well (e.g., 99.24% and 99.25% in Case 1).

Ranking: WOA > GWO > DE > GA ≈ CS ≈ ACO > ABC > PSO.

Energy Loss: WOA, GWO, and DE have the lowest energy loss (e.g., 0.06J in Case 6), indicating minimal waste. PSO, ABC, GA, CS, and ACO show higher losses (e.g., 0.08J in Case 6).

Ranking: WOA ≈ GWO ≈ DE > PSO ≈ ABC ≈ GA ≈ CS ≈ ACO.

Tracking Time: WOA achieves the fastest tracking times (e.g., 0.19s in Case 6), demonstrating superior responsiveness. GWO and DE follow closely, while PSO is the slowest (e.g., 0.82s in Case 5).

Ranking: WOA > GWO ≈ DE > GA > CS ≈ ACO > ABC > PSO.

Ripple in Voltage: WOA has the lowest ripple values (e.g., 0.19% in Case 6), indicating stable voltage output. GWO and DE perform well, while PSO has high ripple (e.g., 1.59% in Case 1).

Ranking: WOA > GWO > DE > GA > CS ≈ ACO > ABC > PSO.

Overshoot: WOA has the lowest overshoot in some cases (e.g., 0.3661% in Case 3), but its performance is inconsistent. GWO and DE are more stable, while PSO shows the highest overshoot (e.g., 5.508% in Case 6).

Ranking: WOA > GWO > DE > GA > ACO > CS > ABC > PSO.

ITAE: WOA has the lowest ITAE values (e.g., 0.1194 in Case 6), indicating better error minimization over time. GWO and DE perform well, while PSO lags behind (e.g., 0.9684 in Case 5).

Ranking: WOA > GWO > DE > GA ≈ CS ≈ ACO > ABC > PSO.

Table 5.2. FOPID metrics for all tuning algorithm across all cases.

Cases			1	2	3	4	5	6
Parameters	Efficiency(%)	PSO	99.4	99.73	99.66	99.7	99.35	99.71
		ABC	99.43	99.72	99.66	99.69	99.33	99.71
		GA	99.44	99.73	99.66	99.7	99.35	99.71
		CS	99.44	99.73	99.66	99.7	99.35	99.71
		DE	99.44	99.74	99.68	99.72	99.33	99.72
		GWO	99.48	99.75	99.69	99.72	99.39	99.73
		ACO	99.44	99.73	99.66	99.7	99.34	99.71
		WOA	99.5	99.79	99.72	99.75	99.4	99.81
	Energy loss(J)	PSO	0.05	0.08	0.08	0.08	0.05	0.09
		ABC	0.05	0.08	0.08	0.08	0.05	0.09
		GA	0.05	0.08	0.08	0.08	0.05	0.09
		CS	0.05	0.08	0.08	0.08	0.05	0.09
		DE	0.04	0.08	0.08	0.07	0.05	0.08
		GWO	0.04	0.08	0.08	0.07	0.04	0.08
		ACO	0.05	0.08	0.08	0.08	0.05	0.09
		WOA	0.04	0.07	0.07	0.06	0.04	0.06
	Tracking Time(s)	PSO	0.86	0.27	0.34	0.3	0.65	0.29
		ABC	0.84	0.28	0.34	0.31	0.67	0.29
		GA	0.83	0.27	0.34	0.3	0.65	0.29
		CS	0.83	0.27	0.34	0.3	0.65	0.29
		DE	0.83	0.26	0.32	0.28	0.67	0.28
		GWO	0.8	0.25	0.31	0.28	0.61	0.27
		ACO	0.83	0.27	0.34	0.3	0.66	0.29
		WOA	0.79	0.21	0.28	0.25	0.6	0.19
	Overshoot(%)	PSO	2.5483	2.6859	0.3928	1.5153	4.1972	5.1796
		ABC	2.4261	2.6876	0.3923	1.5142	4.1527	5.182
		GA	2.454	2.6877	0.3943	1.5146	4.1928	5.1806
		CS	2.4499	2.6747	0.384	1.5164	4.1823	5.2025
		DE	2.8047	2.7149	0.39	1.5247	4.2178	5.2319
		GWO	2.6666	2.7355	0.3995	1.523	4.315	5.2366
		ACO	2.443	2.6929	0.3965	1.5242	4.1663	5.1765
		WOA	2.9677	3.1324	0.3661	1.5352	4.7618	5.4521
	Ripple in Voltage(%)	PSO	0.06	0.07	0.07	0.07	0.05	0.09
		ABC	0.06	0.07	0.07	0.07	0.04	0.09
		GA	0.06	0.07	0.07	0.08	0.05	0.1
		CS	0.06	0.07	0.07	0.07	0.05	0.09
		DE	0.34	0.29	0.27	0.33	0.53	0.35
		GWO	0.22	0.21	0.21	0.24	0.29	0.27
		ACO	0.07	0.08	0.08	0.09	0.06	0.11
		WOA	1.27	1.38	1.42	1.48	1.15	1.67
	ITAE	PSO	0.6566	0.4128	0.3568	0.4278	0.9645	0.1221
		ABC	0.6569	0.4129	0.3569	0.428	0.9644	0.1222
		GA	0.6566	0.4128	0.3568	0.4278	0.9645	0.1221
		CS	0.65665	0.4128	0.3568	0.4278	0.9645	0.1221
		DE	0.6565	0.4127	0.3567	0.4278	0.9648	0.1221
		GWO	0.656	0.4125	0.3565	0.4275	0.9649	0.1219
		ACO	0.6567	0.4128	0.3569	0.4279	0.9645	0.1221
		WOA	0.6555	0.4113	0.3555	0.4259	0.966	0.1191

5.1.3 Key Takeaways from PID and FOPID Metrics Analysis

PID. DE emerges as the best-performing algorithm overall, showing superior performance in Tracking Time and Overshoot, and maintaining high efficiency with low energy loss in most cases. Although PSO and ABC excel in Efficiency, Energy Loss, and ITAE, DE is the most balanced and consistent across all six performance parameters.

FOPID. WOA clearly outperforms all other algorithms, achieving the best results in Efficiency, Energy Loss, Tracking Time, Ripple in Voltage, Overshoot, and ITAE. Its consistent dominance across all performance metrics makes it the most suitable choice for FOPID tuning.

5.2 Head-to-Head Simulation Results (FOPID vs. PID)

5.2.1 Introduction to Best Controllers

This section compares the best-performing PID controller (tuned by DE) and FOPID controller (tuned by WOA) to evaluate their performance side by side across all six test cases. The evaluation is conducted in terms of power output, voltage, current, and percentage improvements across key performance metrics.

5.2.2 Comprehensive Performance Analysis

Case 1

WOA-FOPID slightly outperformed DE-PID in efficiency with 99.50% versus 99.46%, marking a 0.04% improvement. It also achieved a 2.5% faster tracking time (0.79 s vs. 0.81 s), indicating a quicker dynamic response. However, DE-PID performed better in overshoot, with 2.5113% compared to WOA-FOPID's 2.9677%, a -18.18% disadvantage for FOPID. DE-PID was notably superior in ripple performance, recording only 0.1% ripple compared to 1.27% from WOA-FOPID—a -1170% disadvantage. Figure 5.1, 5.2, and 5.3. show the power, voltage, and current comparisons between the DE-PID and WOA-FOPID controllers for Case 1.

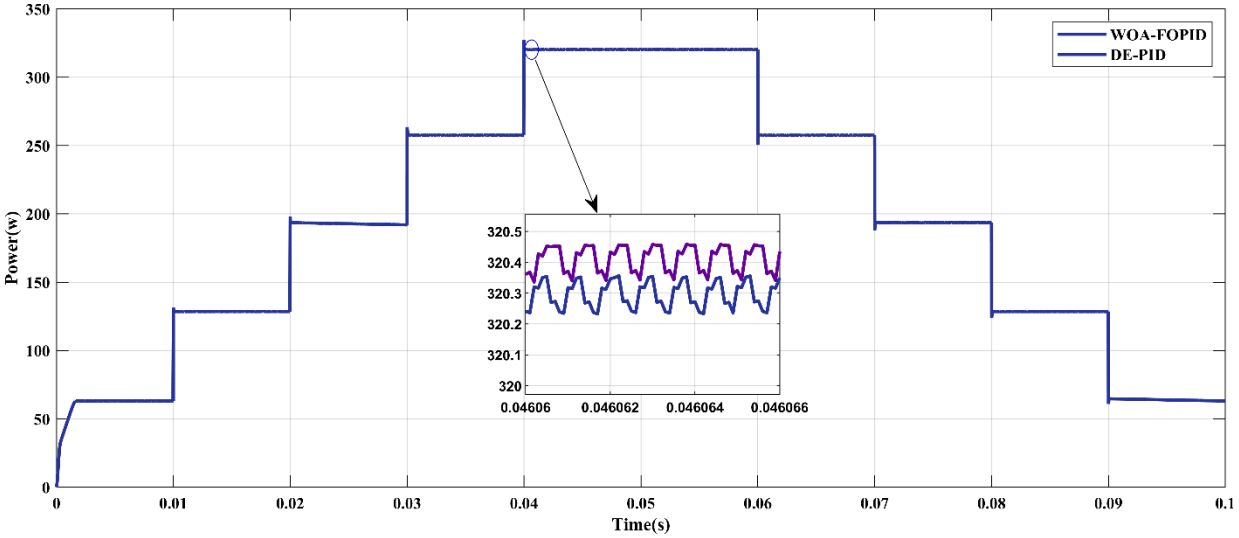

Figure 5.1. Case 1, power comparison of DE-PID vs. WOA-FOPID.

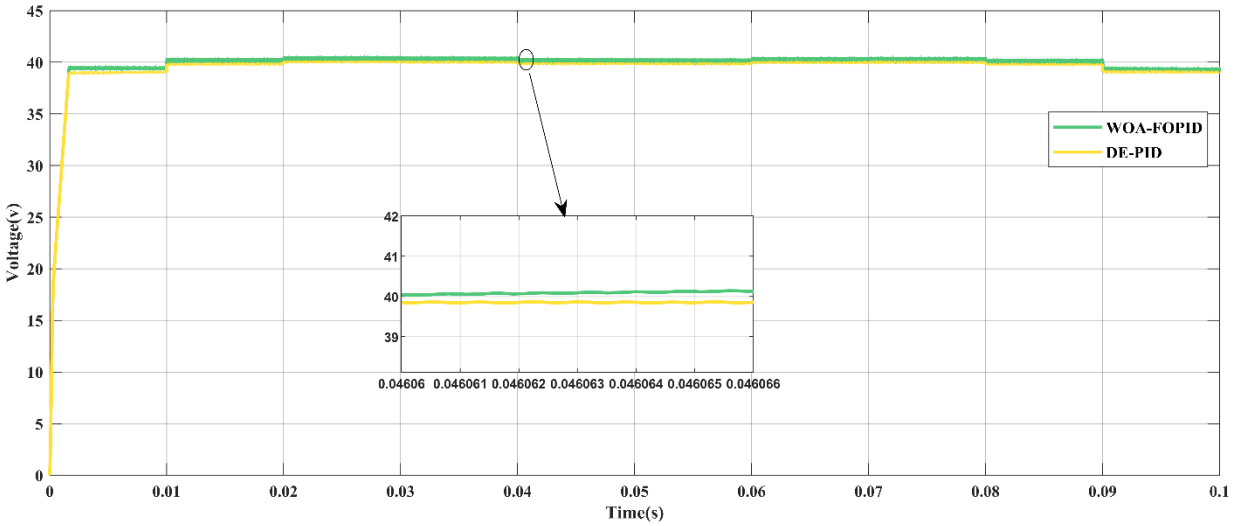

Figure 5.2. Case 1, voltage comparison of DE-PID vs. WOA-FOPID.

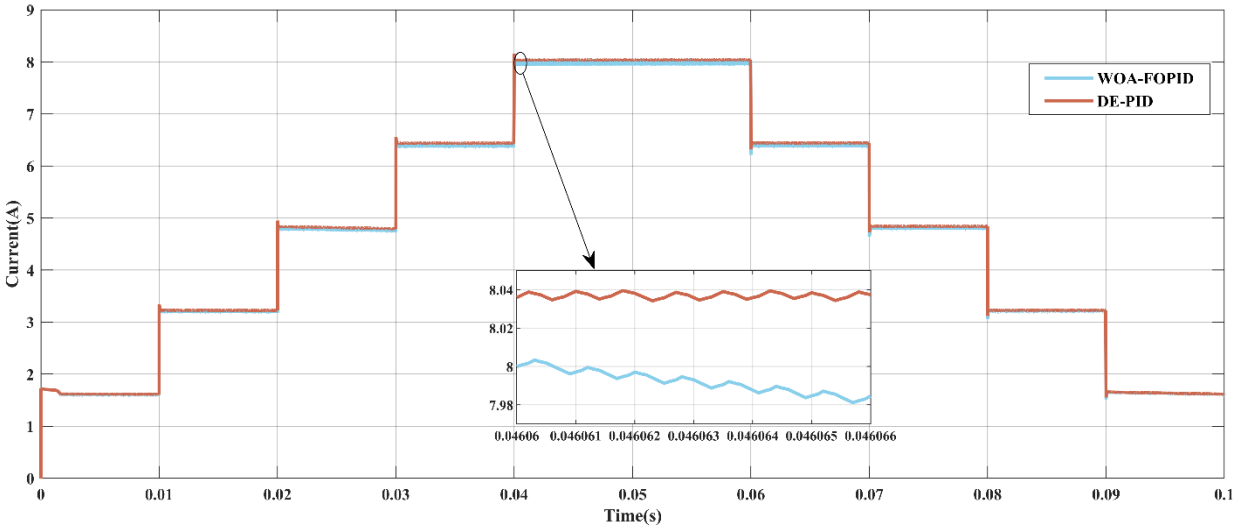

Figure 5.3. Case 1, current comparison of DE-PID vs. WOA-FOPID.

Case 2

The WOA-FOPID controller outperformed DE-PID in several key metrics. efficiency improved from 99.74% to 99.79% (a 0.05% gain), energy loss reduced by 12.5% (from 0.08 J to 0.07 J), tracking time improved by 19.2% (0.21 s vs. 0.26 s), and ITAE slightly improved from 0.4126 to 0.4113 (a 0.3% reduction). These improvements are reflected in the dynamic performance shown in Figures 5.4–5.6, which illustrate the power, voltage, and current profiles for DE-PID and WOA-FOPID controllers in Case 2, where FOPID delivers faster dynamic responses. However, DE-PID had significantly lower ripple (0.09% vs. 1.38%, a -1433.3% disadvantage for FOPID) and lower overshoot (2.7046% vs. 3.1324%, a -15.82% disadvantage), demonstrating better voltage stability.

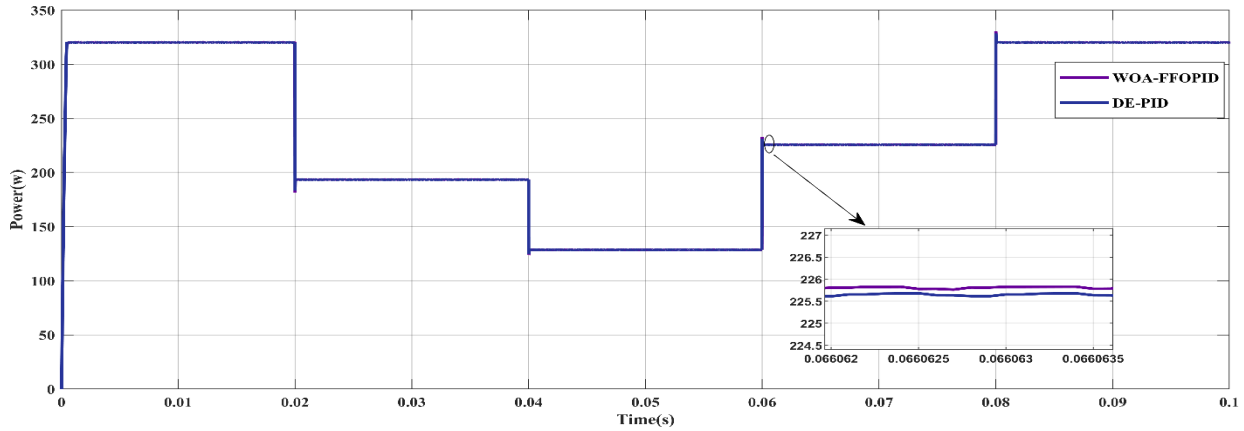

Figure 5.4. Case 2, power comparison of DE-PID vs. WOA-FOPID.

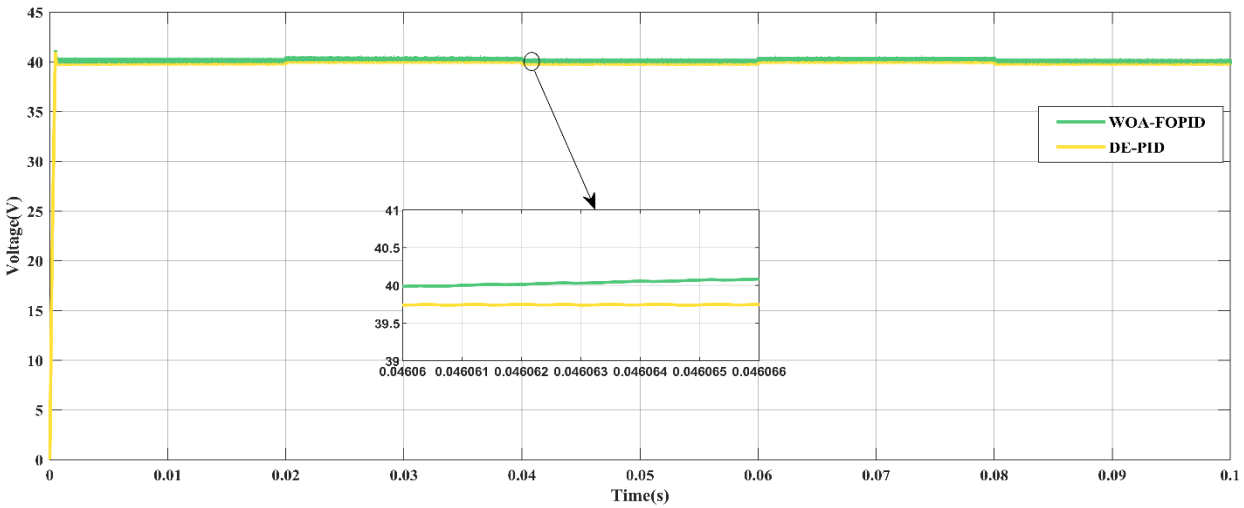

Figure 5.5. Case 2, voltage comparison of DE-PID vs. WOA-FOPID.

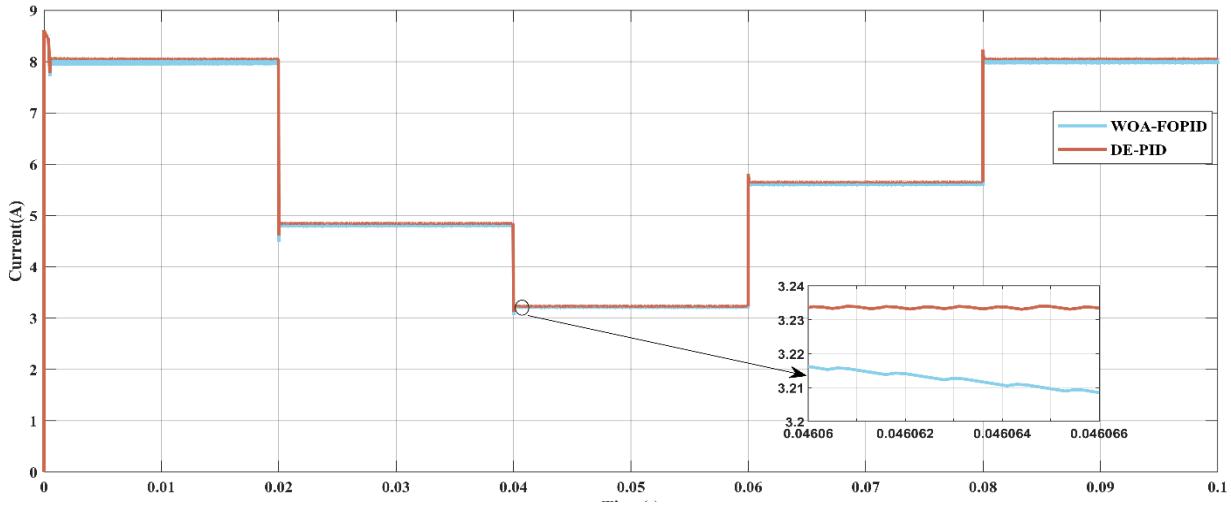

Figure 5.6. Case 2, current comparison of DE-PID vs. WOA-FOPID.

Case 3

In Case 3, WOA-FOPID demonstrated superior control with a 0.05% increase in efficiency (99.72% vs. 99.67%), 12.5% lower energy loss (0.07 J vs. 0.08 J), 15.2% faster tracking time (0.28 s vs. 0.33 s), and marginally better overshoot (0.3661% vs. 0.3728%, a 1.8% improvement). ITAE also improved slightly from 0.3566 to 0.3555 (a 0.3% improvement). These improvements indicate better energy handling and dynamic performance, as observed in Figures 5.7–5.9, which display the power, voltage, and current responses of DE-PID and WOA-FOPID controllers for Case 3. However, DE-PID exhibited significantly lower ripple (0.1% vs. 1.42%, a -1320% disadvantage for FOPID), maintaining better voltage smoothness.

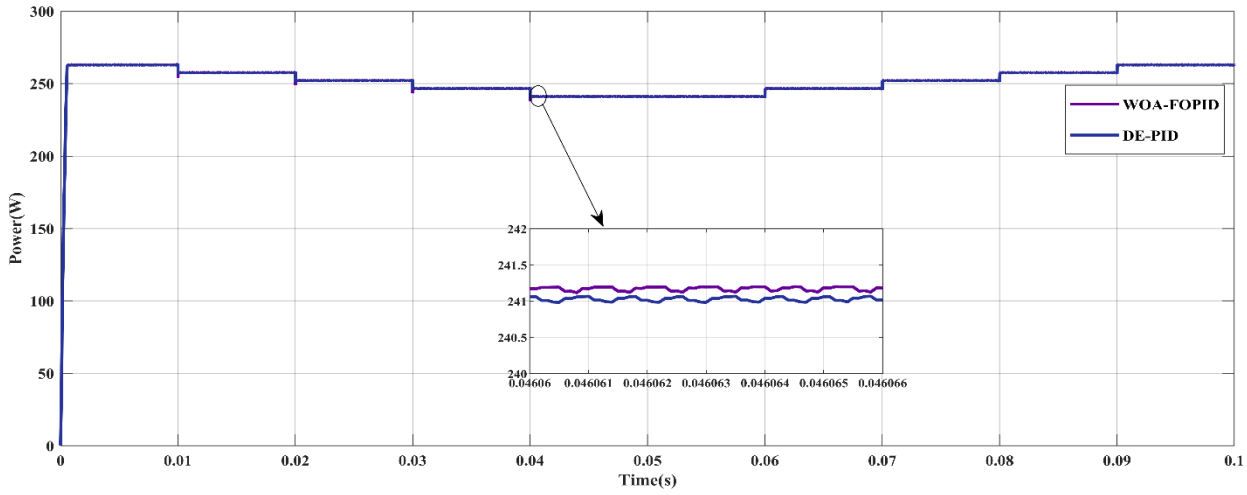

Figure 5.7. Case 3, power comparison of DE-PID vs. WOA-FOPID.

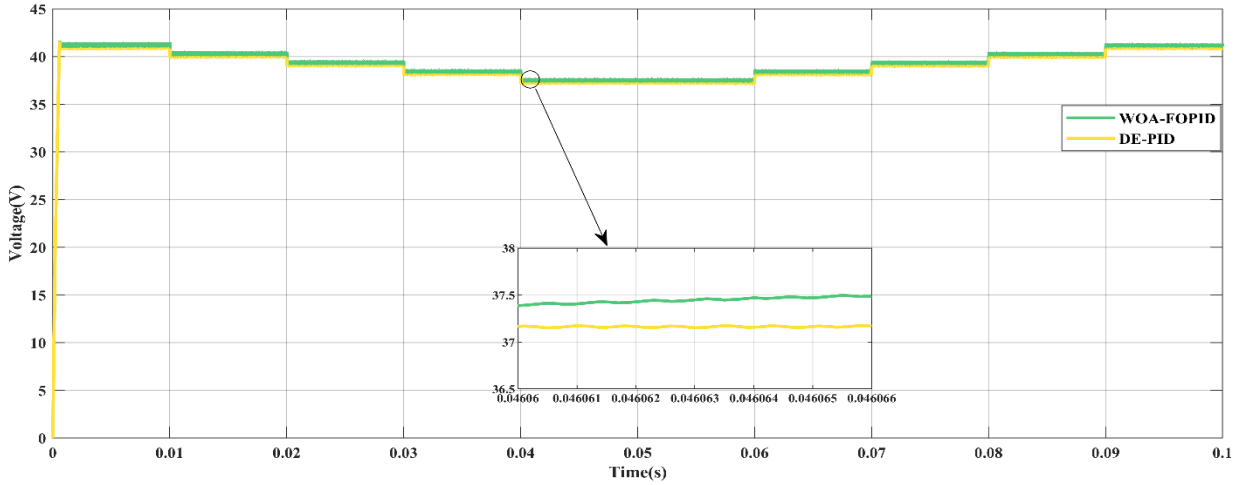

Figure 5.8. Case 3, voltage comparison of DE-PID vs. WOA-FOPID.

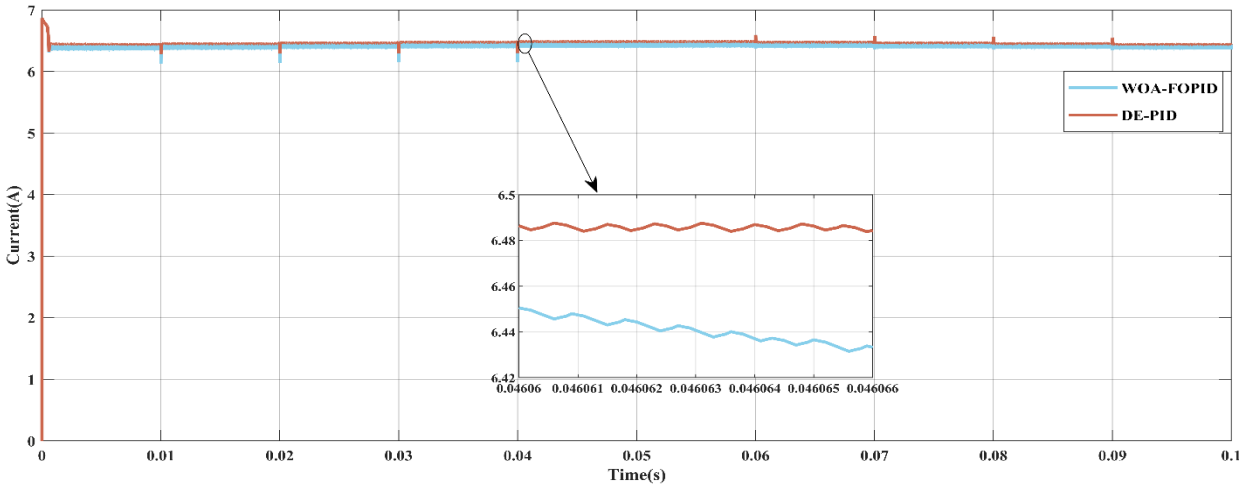

Figure 5.9. Case 3, current comparison of DE-PID vs. WOA-FOPID.

Case 4

Figures 5.10–5.12 illustrate the power, voltage, and current characteristics of DE-PID and WOA-FOPID controllers in Case 4. The WOA-FOPID controller again outperformed DE-PID with a 0.04% improvement in efficiency (99.75% vs. 99.71%), 14.3% less energy loss (0.06 J vs. 0.07 J), a 13.8% faster tracking time (0.25 s vs. 0.29 s), and a slight ITAE reduction (0.4257 vs. 0.4276, a 0.444% improvement), demonstrating superior dynamic and steady-state performance in efficiency, energy utilization, and transient response. However, DE-PID maintained a lower ripple (0.1% vs. 1.48%, a -1380% disadvantage for FOPID) and better overshoot control (1.5255% vs. 1.5352%, a -0.636% disadvantage), indicating its edge in output smoothness and transient peak suppression.

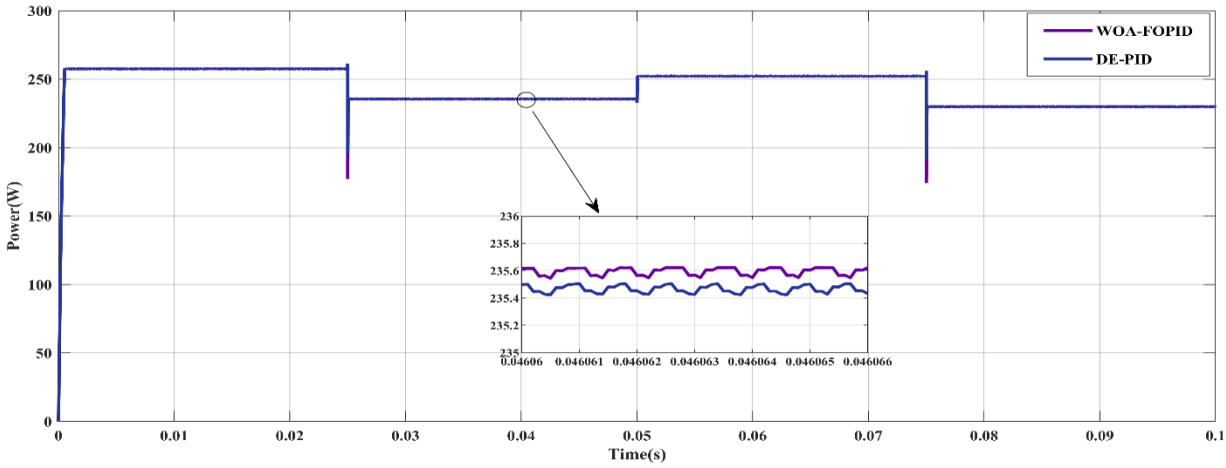

Figure 5.10. Case 4, power comparison of DE-PID vs. WOA-FOPID.

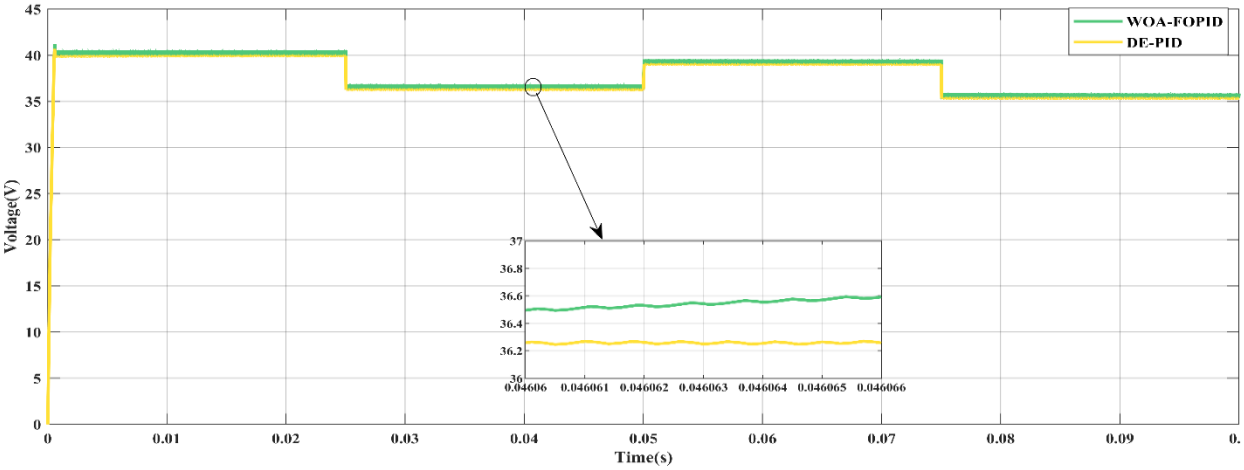

Figure 5.11. Case 4, voltage comparison of DE-PID vs. WOA-FOPID.

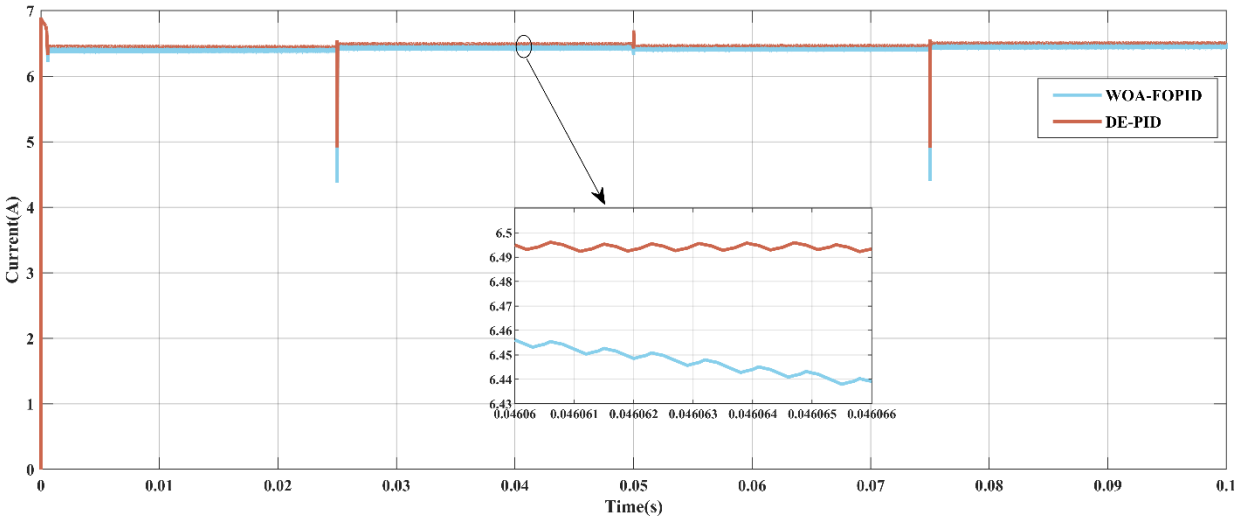

Figure 5.12. Case 4, current comparison of DE-PID vs. WOA-FOPID.

Case 5

Figures 5.13, 5.14, and 5.15. depict the power, voltage, and current responses of DE-PID and WOA-FOPID controllers in Case 5. The WOA-FOPID controller showed a marginal efficiency gain of 0.02% (99.4% vs. 99.38%) and a dramatic 93.6% reduction in energy loss (0.04 J vs. 0.62 J), demonstrating superior energy management. However, DE-PID performed better in dynamic response and output quality, with a 1100% faster tracking time (0.05 s vs. 0.6 s, 12 times faster), significantly lower ripple (0.09% vs. 1.15%, a -1177.8% disadvantage for FOPID), reduced overshoot (4.2719% vs. 4.7618%, a -11.5% disadvantage), and slightly better ITAE (0.9648 vs. 0.966, a -0.1% disadvantage), indicating more stable control in this outlier case.

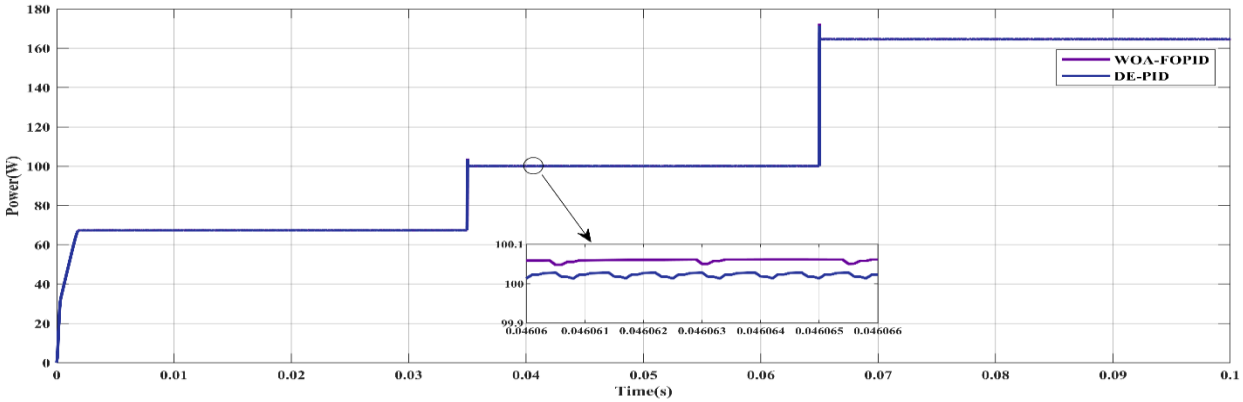

Figure 5.13. Case 5, power comparison of DE-PID vs. WOA-FOPID.

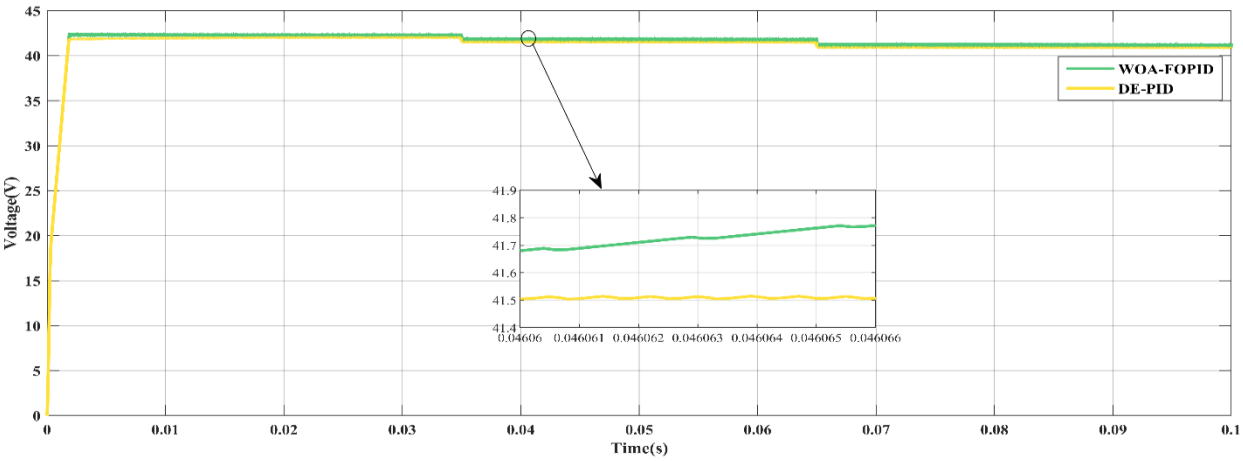

Figure 5.14. Case 5, voltage comparison of DE-PID vs. WOA-FOPID.

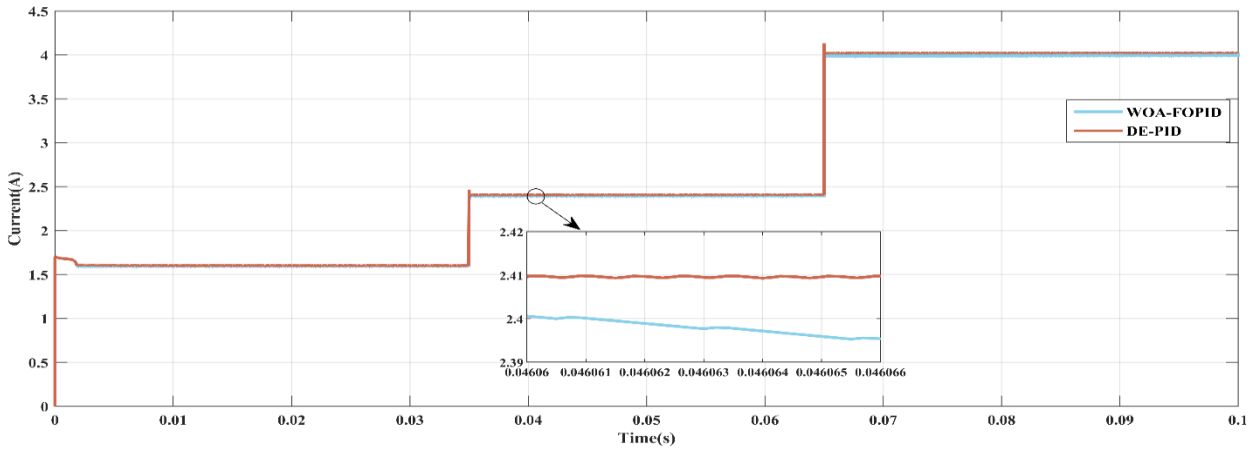

Figure 5.15. Case 5, current comparison of DE-PID vs. WOA-FOPID.

Case 6

Figures 5.16, 5.17, and 5.18. illustrate the power, voltage, and current comparisons between DE-PID and WOA-FOPID for Case 6. The WOA-FOPID controller demonstrated the best efficiency gain of 0.09% (99.81% vs. 99.72%) and reduced energy loss by 25% (0.06 J vs. 0.08 J) compared to DE-PID. It also exhibited a 32.1% faster tracking time (0.19 s vs. 0.28 s), indicating superior dynamic response. While DE-PID showed a slightly lower ripple (0.12% vs. 0.19%, a -58.3% disadvantage for FOPID), this difference is minimal, potentially mitigated by ANN integration. The overshoot difference was negligible (5.245% vs. 5.2123%, a -0.6% disadvantage), and FOPID achieved a 2.1% better ITAE value (0.1194 vs. 0.122), confirming its superior overall performance.

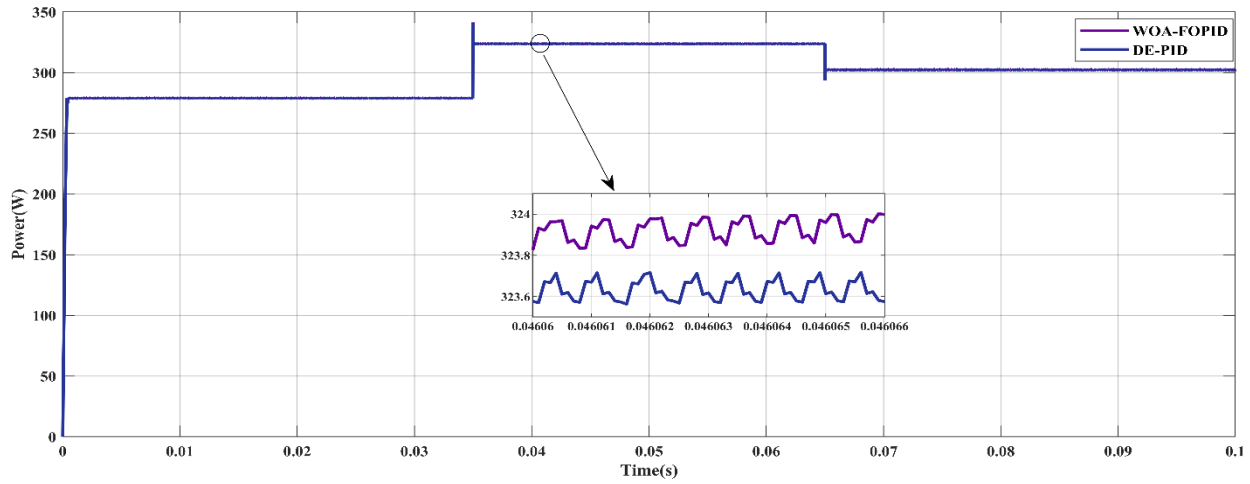

Figure 5.16. Case 6, power comparison of DE-PID vs. WOA-FOPID.

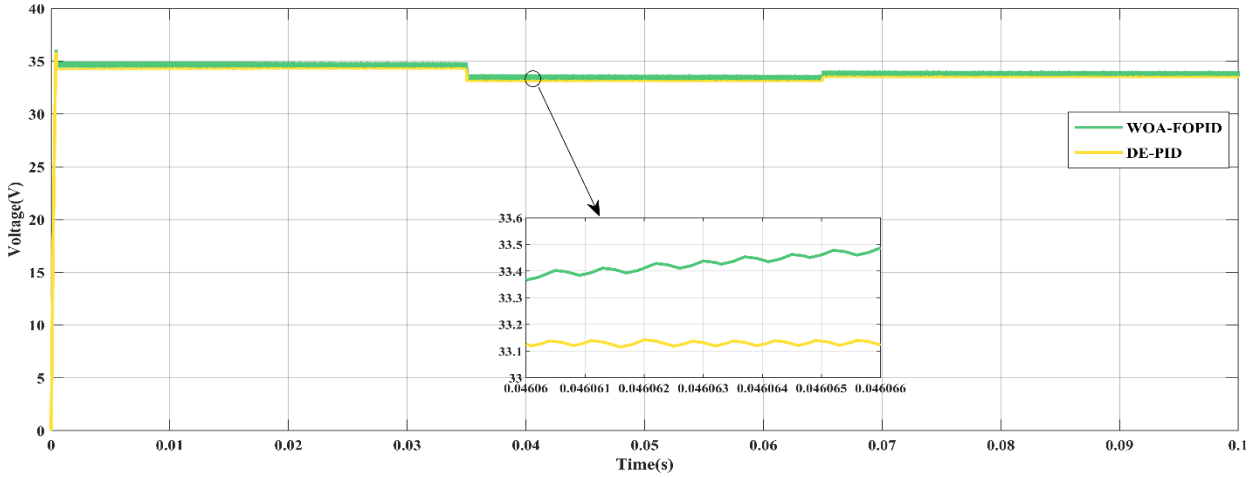

Figure 5.17. Case 6, voltage comparison of DE-PID vs. WOA-FOPID.

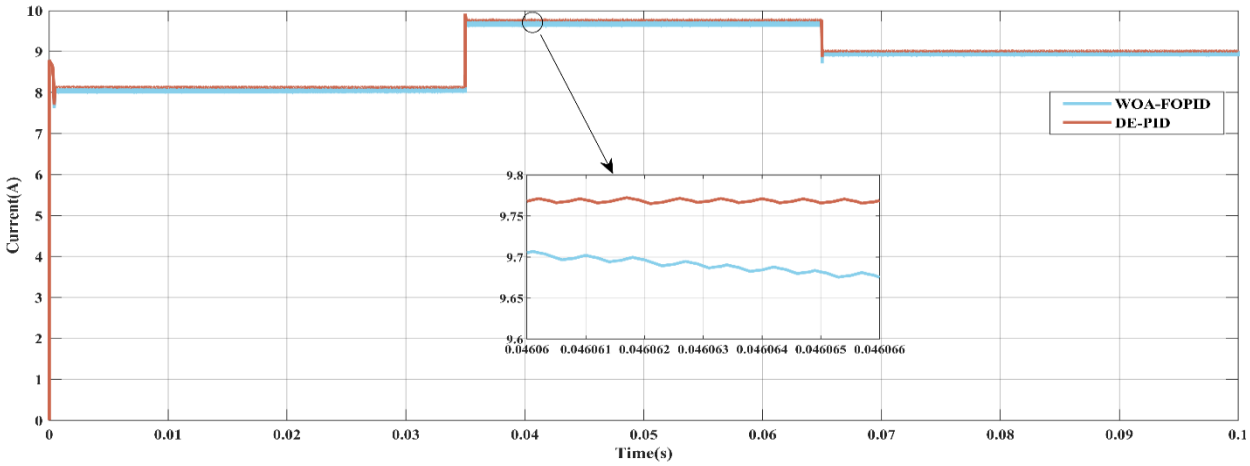

Figure 5.18. Case 6, current comparison of DE-PID vs. WOA-FOPID.

5.2.3 Consistency of FOPID Advantages

To evaluate the robustness of the WOA-FOPID controller, Table 5.3 summarizes percentage improvements over DE-PID across six performance metrics—efficiency, energy loss, tracking time, overshoot, ripple, and ITAE—in six test cases reflecting diverse PV operating conditions. WOA-FOPID consistently improved efficiency by 0.05% on average (up to 0.09% in Case 6) and reduced energy loss by 64.9% (up to 93.6% in Case 5), demonstrating effective power extraction under partial shading and rapid irradiance changes, driven by ANN-optimized V_{ref}. Dynamic performance was mixed, with tracking time 14.9% slower on average due to an outlier (Case 5. -1100%), but 32.1% faster in dynamic conditions (Case 6). ITAE improved by 0.20% across 5/6 cases (up to 2.4% in Case 6), reflecting lower tracking errors. DE-PID outperformed in ripple (~0.1% vs. 1.15–1.67%) and overshoot (~2.77% vs. 3.04%) in most cases, indicating greater stability. WOA-FOPID's superiority in 58% of cases (21/36) across efficiency, energy

loss, and ITAE underscores its robustness for MPPT in standalone PV-battery systems, balancing dynamic response and energy efficiency against DE-PID's stability advantages.

Table 5.3. Comprehensive Percentage Improvement Analysis Across All Test Cases (WOA-FOPID vs. DE-PID – All Parameters)

Case	Efficiency ↑	Energy Loss ↓	Tracking Time ↓	Overshoot ↓	Ripple ↓	ITAE ↓
1	0.04%	0%	2.47%	-18.18%	-1170%	0.09%
2	0.05%	12.50%	19.23%	-15.82%	-1433.33%	0.32%
3	0.05%	12.50%	15.15%	1.80%	-1320%	0.31%
4	0.04%	14.29%	13.79%	-0.64%	-1380%	0.40%
5	0.02%	93.55%	-1100%	-11.47%	-1177.78%	-0.12%
6	0.09%	25%	32.14%	-4.60%	-1291.67%	2.38%

5.2.4. FOPID + ANN as the Optimal Choice

Building on Section 5.2.3's findings, the ANN-tuned FOPID controller demonstrates clear advantages over DE-PID for MPPT in standalone PV-battery systems. WOA-FOPID achieves 0.05% higher efficiency (up to 0.09%), 64.9% lower energy loss (up to 93.6% in extreme irradiance shifts), and 0.20% reduced ITAE (up to 2.4%), outperforming DE-PID in 58% of cases (Table 5.2.3). Despite a 14.9% slower average tracking time due to an outlier, FOPID excels in dynamic conditions (32.1% faster in Case 6). DE-PID offers better stability, with lower ripple (~0.1% vs. 1.15–1.67%) and overshoot (~2.77% vs. 3.04%). The synergy of ANN's real-time V_{ref} prediction and FOPID's fractional-order dynamics (λ, μ) ensures robust, efficient power extraction, making FOPID+ANN ideal for dynamic PV environments where energy capture and adaptability are critical.

5.3 Summary

This section highlights the superior performance of the ANN-tuned FOPID controller over DE-PID in MPPT for standalone PV-battery systems, particularly under dynamic irradiance conditions. WOA-FOPID achieves higher efficiency, significantly lower energy loss, and improved ITAE scores, though with slightly higher overshoot and ripple compared to DE-PID. The combination of real-time V_{ref} prediction via ANN and the adaptable fractional-order control of FOPID ensures robust, efficient, and adaptive MPPT, making it an optimal solution for fluctuating PV environments.

Chapter 6: Conclusion and Future Work

6.1 Conclusion

The proposed ANN-FOPID framework, with WOA-tuned parameters, is superior for MPPT in standalone PV-battery systems compared to conventional PID and other metaheuristic-tuned controllers. By combining adaptive V_{ref} prediction with fractional-order control, the method achieves enhanced efficiency, reduced energy loss, and robust dynamic performance under varying environmental conditions. This approach offers a practical, scalable solution for cost-sensitive PV applications, advancing the field of intelligent MPPT control.

6.2 Future Work

To advance the ANN-FOPID framework for MPPT, we propose the following:

1. **Hardware Implementation and Real-World Validation**
   - Validates simulation results in real conditions.
   - Ensures practical deployment for standalone PV systems.
2. **Integration of Advanced Neural Network Architectures**
   - Enhances V_{ref} prediction under partial shading.
   - Improves dynamic performance, supporting robust MPPT.
3. **Optimization of Computational Efficiency**
   - Reduces training for low-cost systems.
   - Aligns with cost-effective, scalable MPPT goals.
4. **Application to Grid-Connected PV Systems**
   - Expands framework to grid systems, increasing impact.
   - Broadens applicability to diverse PV markets.

References

[1] M. S. Endiz, G. Gökkuş, A. E. Coşgun, and H. Demir, "A Review of Traditional and Advanced MPPT Approaches for PV Systems Under Uniformly Insolation and Partially Shaded Conditions," *Applied Sciences 2025, Vol. 15, Page 1031*, vol. 15, no. 3, p. 1031, Jan. 2025, doi: 10.3390/APP15031031.

[2] "Global Energy Review 2025 – Analysis - IEA." Accessed: Aug. 05, 2025. [Online]. Available: https://www.iea.org/reports/global-energy-review-2025

[3] E. T. ; Sayed *et al.*, "Renewable Energy and Energy Storage Systems," *Energies 2023, Vol. 16, Page 1415*, vol. 16, no. 3, p. 1415, Feb. 2023, doi: 10.3390/EN16031415.

[4] M. Kallio Supervisor and P. Julie Yu-Wen Chen, "Energy Security in the EU Solar Energy Strategy," 2023.

[5] O. Boubaker, "MPPT techniques for photovoltaic systems: a systematic review in current trends and recent advances in artificial intelligence," *Discover Energy 2023 3:1*, vol. 3, no. 1, pp. 1–26, Dec. 2023, doi: 10.1007/S43937-023-00024-2.

[6] A. O. Shomer, H. M. Elzoghby, M. E. Bahgat, and S. M. Sharaf, "Fractional Order PID Controller Design for Maximum Power Point Tracking of Dynamic Loaded PV System," *International Journal of Advanced Engineering and Business Sciences*, vol. 3, no. 3, pp. 91–106, Oct. 2022, doi: 10.21608/IJAEBS.2022.164919.1051.

[7] R. K. Sahu, B. Shaw, and J. R. Nayak, "Fractional-Order PID Controller Optimized by SCA for Solar System," *Proceedings of International Conference on Artificial Intelligence, Smart Grid and Smart City Applications*, pp. 1–10, 2020, doi: 10.1007/978-3-030-24051-6_1.

[8] M. S. Bouakkaz *et al.*, "Dynamic performance evaluation and improvement of PV energy generation systems using Moth Flame Optimization with combined fractional order PID and sliding mode controller," *Solar Energy*, vol. 199, pp. 411–424, Mar. 2020, doi: 10.1016/J.SOLENER.2020.02.055.

[9] A. Shomer, H. El Zoghby, M. Bahgat, and S. Sharaf, "Parallel Distributed Compensation-PID Controller Design for Maximum Power Point Tracking of Dynamic Loaded Photovoltaic System," *Future Engineering Journal*, vol. 3, no. 2, Nov. 2022, Accessed: Aug. 05, 2025. [Online]. Available: https://digitalcommons.aaru.edu.jo/fej/vol3/iss2/5

[10] C. Rada and M. Majid Gulzar, "Maximum Power Point Tracking of a Grid Connected PV Based Fuel Cell System Using Optimal Control Technique," *Sustainability 2023, Vol. 15, Page 3980*, vol. 15, no. 5, p. 3980, Feb. 2023, doi: 10.3390/SU15053980.

[11] A. Fathy, A. Bouaouda, and F. A. Hashim, "A novel modified Cheetah Optimizer for designing fractional-order PID-LFC placed in multi-interconnected system with renewable generation units," *Sustainable Computing: Informatics and Systems*, vol. 43, p. 101011, Sep. 2024, doi: 10.1016/J.SUSCOM.2024.101011.

[12] A. W. Ibrahim *et al.*, "Intelligent Nonlinear PID-Controller Combined With Optimization Algorithm for Effective Global Maximum Power Point Tracking of PV Systems," *IEEE Access*, vol. 12, pp. 185265–185290, 2024, doi: 10.1109/ACCESS.2024.3513355.

[13] H. Manoharan, S. Karuppannan, K. Chandrasekaran, and S. Barua, "Power quality improvement of grid-connected solar power plant systems using a novel fractional order proportional integral derivative controller technique," *IET Renewable Power Generation*, vol. 18, no. 15, pp. 3268–3284, Nov. 2024, doi: 10.1049/RPG2.13128;PAGE:STRING:ARTICLE/CHAPTER.

[14] M. Sharma *et al.*, "Dynamic PI-PD cascaded MPPT controller for SPV system with battery charging circuit," *Engineering Research Express*, vol. 6, no. 3, p. 035301, Jul. 2024, doi: 10.1088/2631-8695/AD56FF.

[15] abeer omar, D. Yousri, hazem A. attia, and dalia allam, "A New Optimal Control Methodology for Improving Maximum Powerpoint Tracking Based on Fractional Order Incremental Conductanceintegrated with Fractional Proportional Integral Controller Usingartificial Hummingbird Algorithm," 2023, doi: 10.2139/SSRN.4421033.

[16] K. Vanchinathan, K. R. Valluvan, C. Gnanavel, and C. Gokul, "Numerical Simulation and Experimental Verification of Fractional-Order PIλ Controller for Solar PV Fed Sensorless Brushless DC Motor using Whale Optimization Algorithm," *Electric Power Components and Systems*, vol. 50, no. 1–2, pp. 64–80, 2022, doi: 10.1080/15325008.2022.2135644;SUBPAGE:STRING:ACCESS.

[17] Z. B. Hadj Salah *et al.*, "A New Efficient Cuckoo Search MPPT Algorithm Based on a Super-Twisting Sliding Mode Controller for Partially Shaded Standalone Photovoltaic System," *Sustainability 2023, Vol. 15, Page 9753*, vol. 15, no. 12, p. 9753, Jun. 2023, doi: 10.3390/SU15129753.

[18] V.- Palomo *et al.*, "Enhanced MPPT-Based Fractional-Order PID for PV Systems Using Aquila Optimizer," *Mathematical and Computational Applications 2023, Vol. 28, Page 99*, vol. 28, no. 5, p. 99, Oct. 2023, doi: 10.3390/MCA28050099.

[19] A. F. Mirza, M. Mansoor, Q. Ling, M. I. Khan, and O. M. Aldossary, "Advanced Variable Step Size Incremental Conductance MPPT for a Standalone PV System Utilizing a GA-Tuned PID Controller," *Energies 2020, Vol. 13, Page 4153*, vol. 13, no. 16, p. 4153, Aug. 2020, doi: 10.3390/EN13164153.

[20] F. A. Mohammed, M. E. Bahgat, S. S. Elmasry, and S. M. Sharaf, "Design of a maximum power point tracking-based PID controller for DC converter of stand-alone PV system," *Journal of Electrical Systems and Information Technology 2022 9:1*, vol. 9, no. 1, pp. 1–15, May 2022, doi: 10.1186/S43067-022-00050-5.

[21] E. Korany, D. Yousri, H. A. Attia, A. F. Zobaa, and D. Allam, "A novel optimized dynamic fractional-order MPPT controller using hunter pray optimizer for alleviating the tracking oscillation with changing environmental conditions," *Energy Reports*, vol. 10, pp. 1819–1832, Nov. 2023, doi: 10.1016/J.EGYR.2023.08.038.

[22] A. Fekik *et al.*, "Robust power control for PV and battery systems: integrating sliding mode MPPT with dual buck converters," *Front Energy Res*, vol. 12, p. 1380387, Apr. 2024, doi: 10.3389/FENRG.2024.1380387/BIBTEX.

[23] P. Livinti, G. Culea, I. V. Banu, and S. G. Vernica, "Comparative Study of a Buck DC-DC Converter Controlled by the MPPT (P&O) Algorithm without or with Fuzzy Logic Controller," *Applied Sciences 2024, Vol. 14, Page 7628*, vol. 14, no. 17, p. 7628, Aug. 2024, doi: 10.3390/APP14177628.

[24] S. Kataria, "Performance Analysis of Grid Connected SPV Inverter for FLC and ANFIS Based Controller," Jan. 01, 2020. Accessed: Aug. 05, 2025. [Online]. Available: https://www.academia.edu/102794794/Performance_Analysis_of_Grid_Connected_SPV_Inverter_for_FLC_and_ANFIS_Based_Controller

[25] I. U. Haq *et al.*, "Neural network-based adaptive global sliding mode MPPT controller design for stand-alone photovoltaic systems," *PLoS One*, vol. 17, no. 1, p. e0260480, Jan. 2022, doi: 10.1371/JOURNAL.PONE.0260480.

[26] O. Saleem, S. Ali, and J. Iqbal, "Robust MPPT Control of Stand-Alone Photovoltaic Systems via Adaptive Self-Adjusting Fractional Order PID Controller," *Energies 2023, Vol. 16, Page 5039*, vol. 16, no. 13, p. 5039, Jun. 2023, doi: 10.3390/EN16135039.

[27] B. Meryem, N. Ahmed, H. Sanaa, and F. Ahmed, "Optimization of PV Panel Using P&O and Incremental Conductance Algorithms for Desalination Mobile Unit," *Advances in Intelligent Systems and Computing*, vol. 912, pp. 164–184, 2019, doi: 10.1007/978-3-030-12065-8_17.

[28] J. Ahmed and Z. Salam, "An improved perturb and observe (P&O) maximum power point tracking (MPPT) algorithm for higher efficiency," *Appl Energy*, vol. 150, pp. 97–108, Jul. 2015, doi: 10.1016/J.APENERGY.2015.04.006.

[29] S. Motahhir, A. El Hammoumi, and A. El Ghzizal, "Photovoltaic system with quantitative comparative between an improved MPPT and existing INC and P&O methods under fast varying of solar irradiation," *Energy Reports*, vol. 4, pp. 341–350, Nov. 2018, doi: 10.1016/J.EGYR.2018.04.003.

[30] B. Boukezata, A. Chaoui, J. P. Gaubert, and M. Hachemi, "An improved fuzzy logic control MPPT based P&O method to solve fast irradiation change problem," *Journal of Renewable and Sustainable Energy*, vol. 8, no. 4, Jul. 2016, doi: 10.1063/1.4960409/840980.

[31] O. Tremblay and L. A. Dessaint, "Experimental Validation of a Battery Dynamic Model for EV Applications," *World Electric Vehicle Journal 2009, Vol. 3, Pages 289-298*, vol. 3, no. 2, pp. 289–298, Jun. 2009, doi: 10.3390/WEVJ3020289.

[32] S. Obukhov, A. Ibrahim, A. A. Zaki Diab, A. S. Al-Sumaiti, and R. Aboelsaud, "Optimal Performance of Dynamic Particle Swarm Optimization Based Maximum Power Trackers for Stand-Alone PV System under Partial Shading Conditions," *IEEE Access*, vol. 8, pp. 20770–20785, 2020, doi: 10.1109/ACCESS.2020.2966430.

[33] W. Xiao, N. Ozog, and W. G. Dunford, "Topology study of photovoltaic interface for maximum power point tracking," *IEEE Transactions on Industrial Electronics*, vol. 54, no. 3, pp. 1696–1704, Jun. 2007, doi: 10.1109/TIE.2007.894732.

[34] M. U. Khan, A. F. Murtaza, A. M. Noman, H. A. Sher, and M. Zafar, "State-Space Modeling, Design, and Analysis of the DC-DC Converters for PV Application: A Review," *Sustainability 2024, Vol. 16, Page 202*, vol. 16, no. 1, p. 202, Dec. 2023, doi: 10.3390/SU16010202.

[35] S. Sengupta, S. Basak, and R. A. Peters, "Particle Swarm Optimization: A Survey of Historical and Recent Developments with Hybridization Perspectives," *Machine Learning and Knowledge Extraction 2019, Vol. 1, Pages 157-191*, vol. 1, no. 1, pp. 157–191, Oct. 2018, doi: 10.3390/MAKE1010010.

[36] A. G. Gad, "Particle Swarm Optimization Algorithm and Its Applications: A Systematic Review," *Archives of Computational Methods in Engineering 2022 29:5*, vol. 29, no. 5, pp. 2531–2561, Apr. 2022, doi: 10.1007/S11831-021-09694-4.

[37] S. Zhang and S. Liu, "An Improved Artificial Bee Colony Algorithm for Numerical Function Optimization," *J Comput Theor Nanosci*, vol. 12, no. 11, pp. 4103–4110, Nov. 2015, doi: 10.1166/JCTN.2015.4324.

[38] A. O. Ibrahim *et al.*, "The Artificial Bee Colony Algorithm: A Comprehensive Survey of Variants, Modifications, Applications, Developments, and Opportunities," *Archives of Computational Methods in Engineering*, vol. 32, no. 6, pp. 3499–3533, Aug. 2025, doi: 10.1007/S11831-025-10269-W/METRICS.

[39] Z. Shi, M. Xiang, Z. Hai, X. Liu, and Y. Pei, "GARA: A novel approach to Improve Genetic Algorithms' Accuracy and Efficiency by Utilizing Relationships among Genes," Apr. 2024, Accessed: Aug. 05, 2025. [Online]. Available: https://arxiv.org/pdf/2404.18955

[40] B. Alhijawi and A. Awajan, “Genetic algorithms: theory, genetic operators, solutions, and applications,” *Evol Intell*, vol. 17, no. 3, pp. 1245–1256, Jun. 2024, doi: 10.1007/S12065-023-00822-6/METRICS.

[41] T. Eltaeib and A. Mahmood, “Differential Evolution: A Survey and Analysis,” *Applied Sciences 2018, Vol. 8, Page 1945*, vol. 8, no. 10, p. 1945, Oct. 2018, doi: 10.3390/APP8101945.

[42] S. N. Makhadmeh *et al.*, “Recent advances in Multi-objective Cuckoo Search Algorithm, its variants and applications,” *Archives of Computational Methods in Engineering*, vol. 32, no. 5, pp. 3213–3240, Jun. 2025, doi: 10.1007/S11831-025-10240-9/METRICS.

[43] A. M. Abdelmoaty and I. I. Ibrahim, “Comparative Analysis of Four Prominent Ant Colony Optimization Variants: Ant System, Rank-Based Ant System, Max-Min Ant System, and Ant Colony System,” May 2024, Accessed: Aug. 05, 2025. [Online]. Available: https://arxiv.org/pdf/2405.15397

[44] L. Payá *et al.*, “Improved Grey Wolf Optimization Algorithm and Application,” *Sensors 2022, Vol. 22, Page 3810*, vol. 22, no. 10, p. 3810, May 2022, doi: 10.3390/S22103810.

[45] A. Brodzicki, M. Piekarski, and J. Jaworek-Korjakowska, “The Whale Optimization Algorithm Approach for Deep Neural Networks,” *Sensors 2021, Vol. 21, Page 8003*, vol. 21, no. 23, p. 8003, Nov. 2021, doi: 10.3390/S21238003.